POLITECNICO DI TORINO
Repository ISTITUZIONALE

System-Level Performance of Torque Vectoring Controllers for Electric Vehicles with In-Wheel Motors

Original
System-Level Performance of Torque Vectoring Controllers for Electric Vehicles with In-Wheel Motors / Carvalho Pinheiro, H.D., Carello, M.. - In: SAE INTERNATIONAL JOURNAL OF VEHICLE DYNAMICS, STABILITY, AND NVH. - ISSN 2380-2162. - ELETTRONICO. - 10:4(2026), pp. 1-28. [10.4271/10-10-04-0029]

Availability:
This version is available at: 11583/3014810 since: 2026-08-24T15:48:57Z

Publisher:
SAE International

Published
DOI:10.4271/10-10-04-0029

Terms of use:

This article is made available under terms and conditions as specified in the corresponding bibliographic description in the repository

Publisher copyright

(Article begins on next page)

29 November 2026

SAE INTERNATIONAL

ARTICLE INFO
Article ID: 10-10-04-0029
© 2026 de Carvalho Pinheiro and Carello
doi:10.4271/10-10-04-0029

System-Level Performance of Torque Vectoring Controllers for Electric Vehicles with In-Wheel Motors

***Henrique de Carvalho Pinheiro*[1] *and Massimiliana Carello*[1]**

[1]*Politecnico di Torino, DIMEAS, Italy*

Abstract

Torque Vectoring (TV) is a critical control technology for enhancing the vehicle dynamics and stability of electric vehicles equipped with four-wheel-independent-drive (4WID) systems. A central challenge in TV design is managing the trade-off between maximizing handling performance and minimizing energy consumption, a crucial factor for EV range. While numerous advanced TV control strategies have been proposed, a comprehensive and comparative benchmark of foundational controllers evaluated on a platform that captures this trade-off is notably absent from the literature. Among the numerous TV control strategies proposed in literature, they are typically evaluated using simplified vehicle models that neglect the detailed dynamics and efficiency losses of the electric powertrain. This study addresses this gap by presenting a comprehensive comparison of six distinct TV control strategies—PID, LQR, two first-order Sliding Mode Controls (SMC), and two second-order SMCs. The controllers are evaluated on a high-fidelity, multi-domain simulation platform that integrates a detailed 14-DOF vehicle dynamics model with electro-thermal models of the motors and energy storage system. The findings reveal a clear, quantifiable trade-off between control precision and energy efficiency. The LQR and suboptimal SOSM controllers delivered superior yaw rate tracking and vehicle stability but incurred a measurable energy penalty. In contrast, the PID and continuous FOSM controllers provided a robust balance of performance and efficiency. More than an exercise on application of different control methods, this research highlights the necessity of using integrated simulation methodologies for the practical design and calibration of active chassis systems, ensuring that gains in dynamic performance do not come at an unacceptable cost to vehicle range and powertrain reliability.

History

Received: 20 Aug 2025
Revised: 13 Jan 2026
Accepted: 19 Feb 2026
e-Available: 13 Mar 2026

Keywords

Electric Vehicles, Powertrain Modeling, Torque Vectoring, Handling, Stability, Lateral Dynamics, In-wheel Motors, 4WID, PID, LQR, SMC

Citation

de Carvalho Pinheiro, H. and Carello, M., "System-Level Performance of Torque Vectoring Controllers for Electric Vehicles with In-Wheel Motors," *SAE Int. J. Veh. Dyn., Stab., and NVH* 10(4):2026, doi:10.4271/10-10-04-0029.

ISSN: 2380-2162
e-ISSN: 2380-2170

© 2026 de Carvalho Pinheiro and Carello. Published by SAE International. This Open Access article is published under the terms of the Creative Commons Attribution Non-Commercial License (http://creativecommons.org/licenses/by-nc/4.0), which permits noncommercial use, distribution, and reproduction in any medium, provided that the original author(s) and the source are credited.



1. Introduction

Vehicles with four independent power sources are not a new concept; early works from the late 1990s described the performance of such layouts, focusing on novel electric motors (EMs) and controllers for high-performance electric vehicles (EVs) with four in-wheel motors [1]. This architecture, now commonly referred to as four-wheel-independent-drive (4WID), offers significant potential to optimize vehicle packaging and, most importantly, provides an unprecedented level of control authority over the vehicle's motion through the independent and rapid modulation of torque at each wheel corner.

A primary application of this authority is Torque Vectoring (TV), a control strategy that enhances vehicle handling and stability by generating a corrective yaw moment. This concept is rooted in the principles of Direct Yaw Control (DYC), which emerged as a key technology for improving vehicle maneuverability and safety at the limits of handling [2, 3]. Foundational DYC strategies proposed that the vehicle sideslip angle (β) is a robust indicator of instability and that a yaw-generation mechanism associated with β-estimation, often using on-board tire models, could significantly improve vehicle behavior [4], overcoming the limitations of controllers based on static directional stability. While the first implementations of these DYC strategies relied on active differentials or selective braking actuation [5–7], the ideal application platform was envisioned early on to be 4WID EVs, which could seamlessly combine DYC with longitudinal slip control [8].

The development and comparison of TV control algorithms is a mature field of study, with a vast body of literature exploring various techniques, as surveyed in the state-of-the-art review by [9]. Classic control strategies are well-represented, including Proportional–Integral (PI) controllers for adjusting front/rear and left/right torque bias [10] and the Linear Quadratic Regulator (LQR) for optimal full-state feedback control [11]. Sliding Mode Control (SMC) is another popular and robust choice, with numerous studies exploring first-order SMC (FOSM), SMC with nonlinear disturbance observers (NDOB), and second-order SMC (SOSM) to reduce chattering [12, 13]. The extensive work by De Novellis et al. provided a significant benchmark in the field, comparing various feedback techniques and exploring integral SMC for TV applications [14–20]. Other advanced strategies have also been widely applied, including Model Predictive Control (MPC) and fuzzy logic controllers, often in hierarchical arrangements that combine multiple systems [21–26]. The sheer volume of research, encompassing many other applications and controller variations [27–44], underscores the importance of TV as a key technology for future EVs.

Most of the cited studies evaluate controller performance using simplified vehicle models, which, while effective for analyzing core dynamic behavior, inherently neglect the detailed characteristics of the electric powertrain. Crucial aspects such as the efficiency maps of the EMs, the dynamic voltage response of the battery under heavy load, and the operational limits of the power electronics are only considered in some recent works [45, 46]. This abstraction prevents a holistic assessment, making it impossible to quantify the critical trade-offs between improvements in dynamic handling and factors such as energy consumption, powertrain efficiency, and component stress. Consequently, a controller that appears optimal in a simplified simulation might be impractical or highly inefficient when deployed in a physical system.

This article addresses this gap by presenting a comprehensive comparison of six common TV control strategies—proportional–integral–derivative (PID), LQR, two FOSM variants, and two SOSM variants—evaluated using a high-fidelity, multi-domain simulation platform that integrates a multi-body vehicle dynamics model with detailed electro-thermal models of the powertrain and Energy Storage System (ESS). This integrated approach, based on the "PerfECT design tool" detailed in [47] and briefly described in this article, enables the simultaneous evaluation of vehicle dynamic response, controller effort, and the resulting energy consumption. This provides insights into controller selection and calibration, directly aligning with the need for research that addresses the system integration and practical applications of active wheel corner technologies. To demonstrate the methodology, the controllers are implemented on a validated model of a high-performance battery electric vehicle, modified from its original dual-motor configuration to a 4WID architecture representative of an IWM application.

The main contribution of this article is the development of a comprehensive analysis strategy that explicitly links vehicle handling objectives with electro-thermal constraints based on more detailed ESS, energy management, and powertrain models. This study addresses the limitations of existing literature by deploying a high-fidelity co-simulation environment to evaluate TV strategies not only on their ability to extend the linear handling region but also on their energy demand and component stress.

Through this approach, the research identifies and quantifies a distinct trade-off between the tracking precision offered by optimal controllers, such as LQR and Suboptimal SOSM, and the resulting energy penalties. This methodology establishes a necessary foundation for the design of active chassis systems that ensure dynamic stability without compromising the operational range and reliability of 4WID EVs.

The remainder of this article is organized as follows: Section 2 describes the vehicle modeling approach and the design of the evaluation maneuvers. Section 3 details the implementation of the overarching control architecture and the six specific TV strategies. Section 4 presents and discusses comparative results, with a focus on analyzing the trade-offs between dynamic performance and energy efficiency. Finally, Section 5 provides concluding remarks and outlines directions for future work.

2. Vehicle Modeling and Maneuver Definition

The foundation of this comparative study is a high-fidelity, multi-domain simulation platform designed to capture the complex interplay between vehicle dynamics and electric powertrain performance. Acknowledging that the efficacy of a TV controller is not merely a function of its algorithm but also of its interaction with the physical limitations and efficiencies of the hardware, a co-simulation environment was developed. This platform, based on the "PerfECT Design Tool" methodology presented in [47], integrates a detailed full-vehicle dynamics model in VI-CarRealTime with comprehensive electro-thermal models of the powertrain and ESS implemented in MATLAB/Simulink. This integrated approach is paramount, as it allows for a holistic evaluation that transcends simple yaw rate tracking to include critical, real-world metrics such as energy consumption, component stress, and thermal loading.

2.1. Vehicle Dynamics and Reference Model

The plant model used for all simulations is a validated, 14-degrees-of-freedom (DOF) model of a Tesla Model 3. The main geometric and inertial parameters of the vehicle are reported in Table 1.

This model, fully detailed and experimentally validated in [47], provides a high level of physical realism by incorporating:

- Suspension geometry: The model includes the kinematic and compliance (K&C) characteristics of the front double-wishbone and rear multi-link suspension systems.
- Tire model: Tire forces and moments are calculated using a Pacejka-based tire model that captures nonlinear behavior under high lateral and longitudinal slip, as well as load sensitivity effects (PAC2002).
- Full-vehicle body motion: The 14-DOF structure accounts for all rigid body motions (longitudinal, lateral, vertical, roll, pitch, yaw) as well as the vertical travel and rotation of each of the four wheels.

While this model serves as the virtual testbed, the reference target for the control systems is generated using the well-established bicycle model. This ensures that the controllers are tasked with making the complex, nonlinear vehicle behave like an idealized, neutral-steering counterpart. The governing equations for the reference model are given by

$$M_z = I_z\dot{\gamma} = N_\beta\beta + N_\gamma\gamma + N_\delta\delta \tag{1}$$

TABLE 1 Original Tesla Model 3 model parameters. (Data taken from Ref. [47].)

Parameter	Value	Unit
Wheelbase (l)	2875	mm
Track (t)	1580	mm
Mass LF (m_{LF})	517	kg
Mass RF (m_{RF})	505	kg
Mass LR (m_{LR})	530	kg
Mass RR (m_{RR})	518	kg
Total mass (m)	2070	kg
Unsprung mass front ($m_{U,F}$)	22.7	kg
Unsprung mass rear($m_{U,R}$)	19.5	kg
Sprung mass (m_S)	1985.6	kg
CoG x	1419	mm
CoG y	18	mm
CoG z	468	mm
Inertia around x-axis (I_{xx})	2.65×10^8	kg × mm^2
Inertia around y-axis (I_{yy})	1.04×10^9	kg × mm^2
Inertia around z-axis (I_{zz})	1.69×10^9	kg × mm^2
Inertia on x-y (I_{xy})	3.22×10^6	kg × mm^2
Inertia on x-z (I_{xz})	4.14×10^7	kg × mm^2
Inertia on y-z (I_{yz})	4.15×10^5	kg × mm^2
Tire model	P235/40 R19	—
Tire radius (nominal/loaded)	335.5/318.7	mm
Tire vertical stiffness	300	N/mm
Tire cornering stiffness (F/R)	1020/760	N/°

© de Carvalho Pinheiro and Carello

$$F_y = mV\left(\gamma + \dot{\beta}\right) = Y_\beta\beta + Y_\gamma\gamma + Y_\delta\delta \tag{2}$$

where M_z is the resultant yaw moment, I_z is the yaw moment of inertia of the vehicle, $\dot{\gamma}$ is the yaw rate variation, β is the sideslip angle, γ is the yaw rate, δ is the front steering angle, and N and Y represent the derivatives of stability as defined in [48].

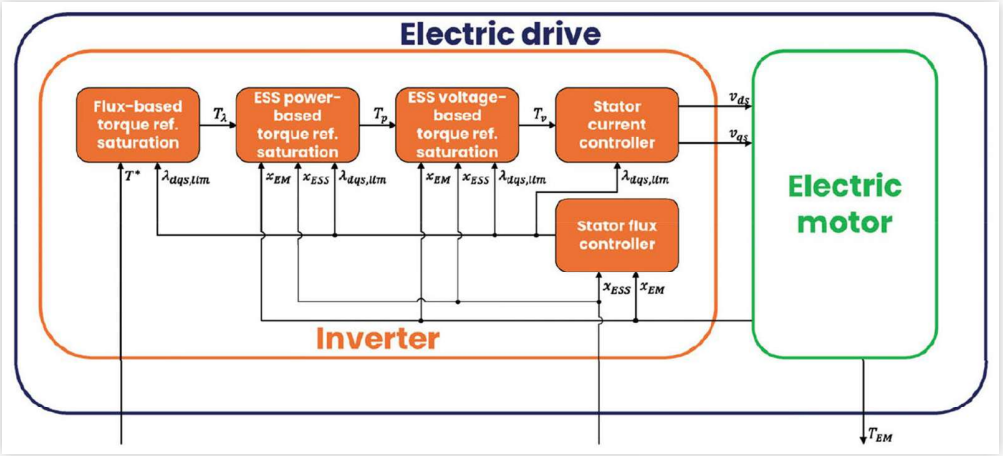
The high-fidelity plant model ensures that the controllers are tested against realistic vehicle dynamics, while the simple reference model provides a clear and consistent performance target that can be implemented in real-time controllers.

2.2. Electric Powertrain and ESS Model

A key contribution of this work lies in the combination of the vehicle dynamics model with detailed modeling of the electric powertrain and ESS, which allows for the analysis of energy consumption and component-level performance.

2.2.1. Electric Motor and Inverter Representation The EMs are modeled as a physics-based representation that captures their efficiency and operational limits.

FIGURE 1 Schematic representation of the electric drive model.



Reprinted with permission from Ref. [50].
© SAGE Publications Ltd.

To avoid the prohibitive computational cost of simulating the high-frequency switching dynamics of the motor controllers, a Maximum Torque Per Ampere (MTPA) strategy is employed [49–51]. For a given torque and speed request coming from the driver, the model uses pre-calculated look-up tables to determine the optimal direct and quadrature axis current commands (i_d, i_q) that minimize ohmic losses. This approach provides a realistic estimation of the motor's dynamics and electrical efficiency across its operating range, accounting for physical limitations and defluxing in the electric machine.

A schematic representation of the saturation process is shown in Figure 1, where a three-step torque saturation process is applied to the torque reference signal, ensuring that the motor's operation remains within the physical constraints imposed by the ESS.

This methodology enables a detailed and accurate simulation of motor currents, voltages, and losses without the prohibitive computational burden of simulating the inverter's high-frequency switching dynamics.

The general equations deployed for the equivalent circuit representation of the electric machines, derived from the obtained values, are given by Equations 3 and 4 that express the voltage and flux equations, respectively.

$$\begin{Bmatrix} V_d \\ V_q \end{Bmatrix} = R_s \begin{Bmatrix} I_d \\ I_q \end{Bmatrix} + \frac{d}{dt} \begin{Bmatrix} \lambda_d \\ \lambda_q \end{Bmatrix} + \omega \begin{bmatrix} 0 & -1 \\ 1 & 0 \end{bmatrix} \begin{Bmatrix} \lambda_d \\ \lambda_q \end{Bmatrix} \tag{3}$$

$$\begin{Bmatrix} \lambda_d \\ \lambda_q \end{Bmatrix} = \begin{bmatrix} L_d & L_{dq} \\ L_{qd} & L_q \end{bmatrix} \begin{Bmatrix} i_d \\ i_q \end{Bmatrix} + \begin{Bmatrix} \lambda_{md} \\ \lambda_{mq} \end{Bmatrix} \tag{4}$$

Furthermore, the model includes a state-based overload management system that mimics the thermal protection logic of a real motor controller. This system tracks the energy dissipated during operation above the motor's continuous power rating. Once a predefined thermal energy threshold is crossed, the controller derates the motor's output to its continuous limit, only allowing peak performance again after a sufficient cool-down period. This feature is critical for realistically simulating performance during extended high-load maneuvers, focusing on system integration and reliability.

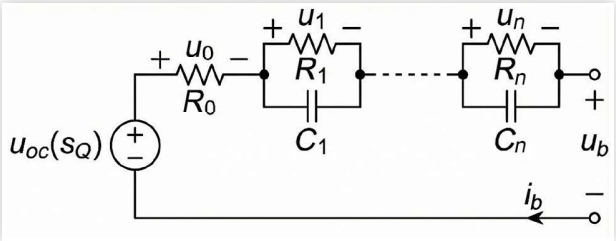
Heat generation in the EMs is calculated by considering mainly copper losses and iron losses [52], as represented in Equations 5 and 6, respectively.

$$P_{copper} = P_{Rs} + P_{Rr} = 3R_s I_{ph}^2 + 3R_r I_r^2 \tag{5}$$

$$P_{iron} = k \cdot V_c \cdot f^m \cdot B^n \tag{6}$$

2.2.2. Battery and BMS Model The ESS is modeled as a dual-polarization Thévenin equivalent circuit (Figure 2), whose parameters are detailed in [47]. This model captures the transient and steady-state voltage response of the battery under dynamic loading. The key parameters—namely open-circuit (V_{OC}), internal resistance (R_0), and the two RC pairs representing polarization effects (R_1, C_1, R_2, C_2)—are implemented as multi-dimensional

FIGURE 2 Dual-polarization Thévenin circuit for electrochemical cell.



© de Carvalho Pinheiro and Carello

TABLE 2 Tesla Model 3 Thévenin parameters varying with SOC during discharge at 25°C. (Data taken from Ref. [47].)

SOC	V_{OC} (V)	R_0 (Ω)	R_1 (Ω)	C_1 (F)	R_2 (Ω)	C_2 (F)
0.00	2.75	0.030	0.0064	200	0.0064	1000
0.10	2.96	0.028	0.0064	250	0.0064	2500
0.20	3.17	0.026	0.0072	750	0.0064	8500
0.30	3.33	0.027	0.0072	1100	0.0064	12,000
0.40	3.53	0.025	0.0072	1450	0.0064	10,000
0.50	3.72	0.023	0.008	1650	0.008	15,000
0.60	3.88	0.024	0.0088	1800	0.0096	21,500
0.70	3.96	0.026	0.0088	2000	0.008	15,000
0.80	4.08	0.027	0.0128	2250	0.0096	15,000
0.90	4.18	0.029	0.024	2100	0.016	22,500
1.00	4.20	0.030	0.0216	2250	0.02	30,000

© de Carvalho Pinheiro and Carello

look-up tables dependent on the battery's state of charge (SOC), temperature, and current direction (charge/discharge).

This level of detail is essential because it accurately models the voltage variations that occur during high current drawing (acceleration) and the voltage swell during high current charging (regenerative braking), meaning the actual voltage supplied to the inverters directly affects the maximum power the motors can deliver (Table 2).

Other than that, by modeling the internal resistances, the model provides a calculation of the energy lost to heat within the battery, which is a driver of overall powertrain inefficiency. Equations 7 and 8 represent the calculation of the pack-level equivalent resistances and capacitances, and the estimation of the heat generated in the ESS.

$$R_{i,eq} = \frac{N_s}{N_p} \cdot R_{i,cell}, \qquad C_{i,eq} = \frac{N_p}{N_s} \cdot R_{i,cell} \tag{7}$$

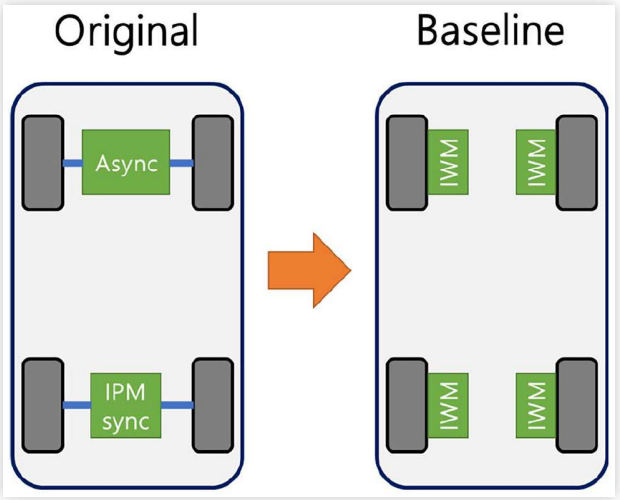
$$Q_{batt} = R_0 i_b^2 + R_1 i_1^2 + R_2 i_2^2 \tag{8}$$

A simplified Battery Management System (BMS) model oversees the ESS, computing SOC evolution and enforcing operational limits on maximum current, maximum power, and minimum/maximum SOC. Other typical BMS tasks, such as fault detection or cell balancing, are not included due to the ESS modeling strategy considering a homogeneous assembly of cells.

2.3. Powertrain Adaptation for 4WID

The original, validated dual-motor vehicle model was adapted to a 4WID configuration to serve as a representative platform for an IWM-equipped vehicle. This "Baseline" layout, shown schematically in Figure 3, assumes an independent motor is directly connected to each wheel.

FIGURE 3 Original and Baseline E-PWT layouts.



© de Carvalho Pinheiro and Carello

The chosen motors for this case study were the EMRAX 268, whose features can be found in the comprehensive technical datasheet provided by the manufacturer [53]. To meet the high-voltage requirements of the EM, the battery pack configuration was virtually modified to double the nominal bus voltage to approximately 720 V by rearranging the number of modules in series and parallel.

The Baseline powertrain characteristics are compared to the Original in Table 3.

A critical consideration for any IWM integration is the increase in unsprung mass. The mass shift and relative inertial adjustments were performed in the VI-CRT environment to accurately represent the added unsprung mass, while no changes were performed in the suspension system.

This additional mass can adversely affect ride comfort and the tire's ability to maintain contact with the road, particularly on uneven surfaces [54, 55]. While some studies highlight these challenges [56, 57], others suggest the effects can be mitigated through advanced suspension design or active control [58–62]. This well-documented trade-off has deep ties to the motivation for this article, as advanced TV control, which leverages the fast

TABLE 3 E-PWT features comparison between Original and Baseline versions.

	Original value	Baseline value
Peak power (kW)	350	640
Peak torque at wheels (Nm)	5850	5500
Continuous power (kW)	200	320
Continuous torque at wheels (Nm)	4383	2343
Maximum wheel speed (rpm)	2000	2000

© de Carvalho Pinheiro and Carello

and precise torque response of IWMs, is a key enabling technology to enhance dynamic stability and potentially counteract any degradation in mechanical grip arising from the increased unsprung mass.

2.4. Maneuver Selection

To ensure a comprehensive comparison, two distinct sets of open-loop maneuvers were implemented. These tests were specifically chosen to probe the vehicle's behavior across its operating envelope, from linear, predictable handling to the nonlinear, near-limit region where control intervention is most critical.

2.4.1. Transient Response Analysis: Step Steering To evaluate the vehicle's transient response, a series of step steer inputs is used. This maneuver is a fundamental test of vehicle stability and represents a simpler and more repeatable alternative to other standardized tests such as the ISO 3888-2 Double Lane Change. By isolating a single, clean steering input, it is possible to precisely analyze key transient metrics, such as rise time, percentage overshoot, and steady-state error, without the compounding effects of the rapid counter-steer found in a full double-lane change, which, in the case of virtual simulation, would also include the dynamics of response of the virtual driver. This provides a clearer and more repeatable basis for comparing the fundamental dynamic performance of the different control algorithms.

As detailed in Table 4, a reference maneuver #1 was established at 70 km/h, and its key parameters were systematically varied to create a family of tests that produce lateral accelerations from moderate to near-limit.

This allows for the evaluation of controller effectiveness across a wide range of operating conditions. The Baseline vehicle's response is shown in Figure 4.

For each one of the maneuvers, it is possible to extract some key response features of the plots, for instance, for maneuver #1, the steady-state lateral acceleration is 0.837 g, and its maximum value accounts for 0.885 g at 2.55 s, representing a 5.73% overshooting. The rising time to achieve 95% of the steady-state value is 0.983 s after the start of the step maneuver, while the settling time in a range of ±2% is 2.462 s.

TABLE 4 Step steering maneuvers.

#	Speed (km/h)	SWA (°)	Step duration (s)
1	70	60	1.0
2	75	60	1.0
3	70	30	1.0
4	70	60	0.5
5	50	60	1.0

© de Carvalho Pinheiro and Carello

2.4.2. Steady-State and Combined-Loading Analysis: Constant Radius Cornering To assess steady-state cornering behavior and quantify the vehicle's understeer characteristics, a series of constant radius cornering (CRC) maneuvers is used. As shown in Table 5, the primary variable is the longitudinal acceleration, which is ramped to force the vehicle through a wide range of combined lateral and longitudinal loading conditions. The radius of the maneuver is kept fixed at 100 m.

The resulting plot of steering angle versus lateral acceleration (Figure 5) provides a clear handling profile.

For the understeering Baseline vehicle, an increasing amount of steering input is required to maintain the cornering radius as lateral acceleration increases. At low speeds (and associated low lateral accelerations), the imposed steering angle represents the kinematic steering condition for the maneuver radius and vehicle wheelbase, while it is also possible to observe the increasing understeering response as the longitudinal acceleration is increased. This maneuver is therefore essential for directly visualizing and quantifying the effectiveness of each controller in achieving its core objective, particularly under the challenging conditions of combined acceleration and cornering.

3. TV Control System

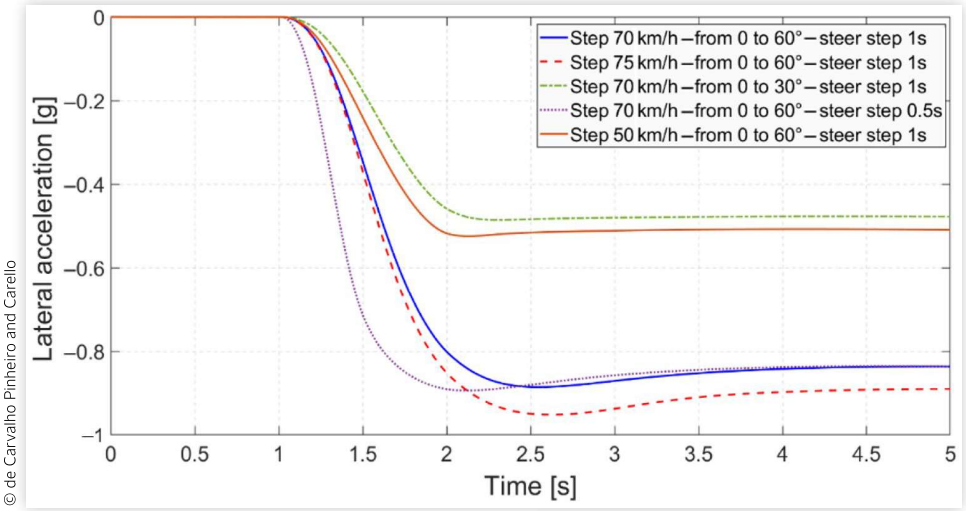
The fundamental goal of the TV system is to improve the vehicle's lateral dynamics by actively modulating the yaw moment. Having established the high-fidelity vehicle model and the evaluation maneuvers, this section details the design and implementation of the TV control system.

3.1. Controller Goals and Performance Evaluation

A complete evaluation framework is essential for a meaningful comparison of control strategies. The framework must not only quantify the achievement of the primary dynamic objectives but also account for the efficiency and feasibility of the control action itself.

3.1.1. Control Objectives As conceptualized in [15], the desired improvements can be summarized as illustrated in the steering angle vs. lateral acceleration plot in Figure 6. In the figure, the original black curve represents a Baseline vehicle without TV, displaying a linear dependence up to around 0.5 g. This Baseline is then improved to the green curve, in which the linear behavior extends until higher lateral accelerations and the maximum observed lateral acceleration reaches the red reference, but maintaining the same slope at the origin. The last curve, in blue, shows a change in the slope, meaning that a lower steering wheel angle (SWA) is needed to achieve

FIGURE 4 Baseline vehicle lateral acceleration during step steering maneuvers.



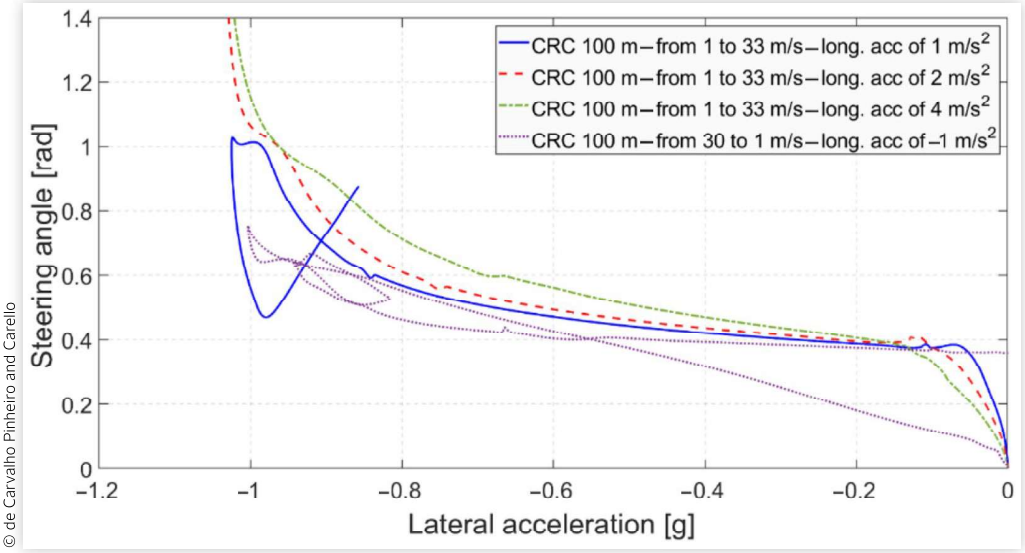
© de Carvalho Pinheiro and Carello

TABLE 5 CRC maneuvers.

#	Initial speed (m/s)	Final speed (m/s)	Ramp duration (s)	Target long. acc. (m/s²)
1	1	33	32	1
2	1	33	16	2
3	1	33	8	4
4	31	1	30	−1

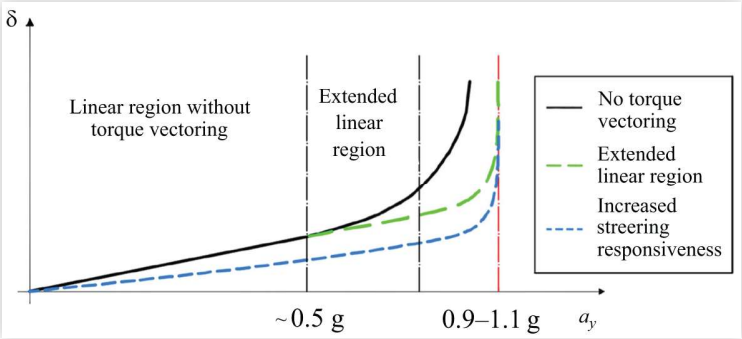
© de Carvalho Pinheiro and Carello

FIGURE 5 Baseline vehicle steering angle vs lateral acceleration during CRC maneuvers.



© de Carvalho Pinheiro and Carello

FIGURE 6 Torque vectoring goals.



Reprinted from Ref. [15] and licensed under the Creative Commons Attribution 4.0 International License (https://creativecommons.org/licenses/by/4.0/_)

a certain level of lateral acceleration. This proposal contains the three primary objectives of a TV system:

1. **Extension of the Linear Handling Region:** To make the vehicle's response more predictable and consistent across a wider range of lateral accelerations.
2. **Increase of Maximum Lateral Acceleration:** To enhance the ultimate grip and stability at the limits of handling.
3. **Improvement in Steering Responsiveness:** To reduce the steering input required for a given cornering maneuver, making the vehicle feel more agile.

These objectives are largely achieved by driving the vehicle's behavior toward a neutral steer characteristic. This ensures a more balanced distribution of lateral forces between the front and rear axles. To this end, the control strategies developed in this study are predominantly yaw-rate-based. The target yaw rate (γ_{ref}) is calculated from the linear bicycle model for a neutral steer vehicle, and the controller's task is to minimize the error between this reference and the actual vehicle yaw rate (γ_{actual}). This approach was chosen over a sideslip-based strategy due to its practical advantages; yaw rate is directly measurable on production vehicles using standard inertial measurement units (IMUs), whereas sideslip angle must be estimated, introducing potential for model mismatch and sensor noise [63–66]. The only exception is the LQR controller, which, due to its full-state feedback nature, inherently includes the sideslip angle in its formulation. For the LQR implementation, it is assumed that the sideslip angle is promptly and precisely estimated by a third-party observer, not modeled.

3.1.2. Performance Metrics A set of quantitative performance metrics was developed to capture the controller's effectiveness in tracking the reference yaw rate and the intensity and efficiency of the control action. The yaw error, e, is defined as

$$e = e_{yaw} = \left(\gamma_{ref} - \gamma_{actual}\right) \tag{9}$$

From this error, three integral-based penalty factors are calculated for each maneuver

$$CP = \int u^2 \, dt \tag{10}$$

$$EP = \int e^2 \, dt \tag{11}$$

$$TEP = \int e^2 \cdot t \, dt \tag{12}$$

Here, CP is the "Control Penalty," where u represents the control output: the corrective yaw moment generated by the unbalanced application of torque between left and right sides of the vehicle. This metric quantifies the total control effort, which is directly correlated with the additional torque demanded from the motors and, consequently, the energy consumed. EP is the "Error Penalty," which measures the cumulative squared error and represents the overall tracking accuracy. TEP is the "Timed Error Penalty," which weights the squared error by time. This metric is particularly useful for penalizing controllers that fail to eliminate steady-state errors during transient maneuvers such as step steering.

These three factors are combined into a single "Overall Penalty" (OP) factor using a weighted sum

$$OP = W_{CP} \cdot \overline{CP} + W_{EP} \cdot \overline{EP} + W_{TEP} \cdot \overline{TEP} \tag{13}$$

For this study, the weights were chosen as $W_{CP} = 0.5$, $W_{EP} = 0.4$, and $W_{TEP} = 0.1$, placing a significant emphasis on control efficiency. To facilitate comparison, the penalty factors for each controller are normalized relative to the performance of the benchmark PID controller in the first maneuver (#1) of each type.

In addition to these integral metrics, several specific performance indicators are extracted from the simulation data to provide further insight:

For Step Steering Maneuvers:

- **(SSE) Steady-state error [-]**—measured as $\gamma_{end}/\gamma_{ideal}$ at the final timestep of the simulation.
- **(OS) Overshoot [-]—**measured as the maximum $\gamma_{actual}/\gamma_{ideal}$, usually just after the step input.
- **ΔSOC [%]**—the percentual variation of the SOC of the battery, representing the overall energy consumption during the maneuver.
- **(Max C) Maximum current [A]**—peak of current requested to the battery during the whole maneuver, proportional to the "stress" put into the system by an aggressive control action.
- **(Max β) Maximum sideslip angle [rad]—**associated to the stability and to the saturation of the tires, reducing the overall β is an accurate indication of the control quality (being one of the goals of the sideslip-based controllers).

For CRC maneuvers:

- **(Max *V*) Maximum speed [km/h]—**maximum longitudinal velocity the vehicle can achieve while maintaining the correct trajectory, indicating a higher grip.
- **(Max a_y) Maximum lateral acceleration [g]—**like the maximum speed (since in a constant radius situation) evaluates the lateral performance directly.
- **(Avg δ) Average steering [rad]—**having as a goal the reactivity of the vehicle, reducing the necessary steering angle to complete the CRC is equivalent to rendering the vehicle "less understeering," which is the Baseline situation of the case study.
- **(Max e_V) Maximum speed error [km/h]—**since during the maneuver the vehicle has a target speed to be followed (based on each case's longitudinal acceleration), any variation represents a failure to keep up with the driver's request.

3.2. Overall Control System Architecture

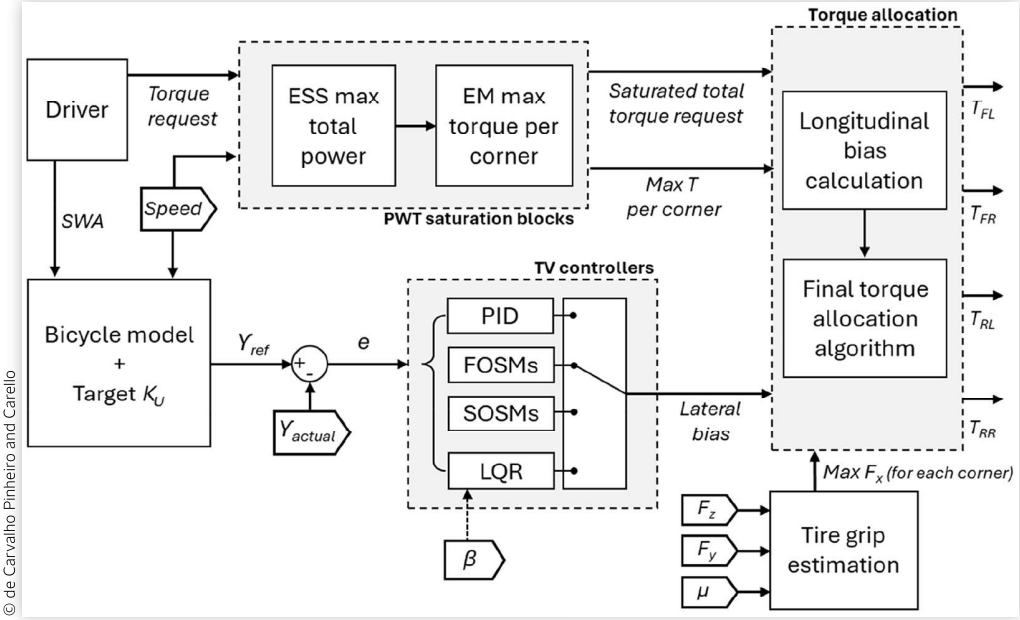
The control system is implemented within the Simulink environment as a hierarchical structure. The architecture can be conceptualized as the high-level block diagram shown in Figure 7.

This diagram illustrates the flow of information from sensor inputs to actuator commands and consists of five main functional blocks:

Reference Yaw Rate Calculator: This block, named "Bicycle mode" in the scheme, receives the vehicle's longitudinal speed (v_x) and the driver's SWA as inputs. It uses the parameters of the linear bicycle model to calculate the ideal yaw rate (γ_{ref}) that corresponds to a target steer response, in this study, a neutral-steering behavior (K_u = 0).

1. **TV Controllers:** This is the core of the system. It takes the reference yaw rate (γ_{ref}) and the actual yaw rate (γ_{actual}) from the vehicle plant model to compute the error, *e*. Based on this error, one of

FIGURE 7 TV control system architecture.



© de Carvalho Pinheiro and Carello

the six control strategies is selected through a switch, and calculates the desired torque lateral bias, which is the primary control output.

2. **Powertrain Saturation:** Before allocation, the total torque requested by the driver is processed to ensure it is feasible. This block receives real-time data on the maximum available power from the BMS and the maximum torque capabilities of each motor (considering MTPA, overload status, and thermal limits) to saturate the requests, preventing commands that the physical system cannot execute.
3. **Tire grip estimation:** Based on the current dynamic state of the vehicle in terms of lateral and longitudinal acceleration, as well as an estimated value of μ for the tire–road conditions, the block estimates the maximum range of longitudinal forces each tire can develop without saturating, by applying the friction ellipse concept.
4. **Torque Allocation:** This final block receives the feasible total longitudinal torque request and the corrective lateral bias. It translates these into individual torque commands for each IWM, guaranteeing that the final torque request won't exceed either the EM maximum torque or the maximum longitudinal force estimated for each corner. For the purposes of this study, an "open-differential" logic is used for the longitudinal bias distribution—meaning that the system tries to equally distribute the torque between front and rear wheels on the same side, whenever possible—to ensure that the observed dynamic changes are a direct result of the TV controller's action.

3.3. Specific Control Strategy Implementations

Six distinct control strategies were implemented and tuned for the 4WID vehicle model.

3.3.1. Proportional–Integral–Derivative Controller The PID controller, a ubiquitous benchmark in industrial and automotive applications, was implemented with set-point weighing on the proportional and derivative terms to mitigate the effect of sharp changes in the reference signal. The control law is given by

$$u = K_P\left(b\cdot\gamma_{ref}-\gamma_{real}\right)+K_I\frac{1}{s}\left(\gamma_{ref}-\gamma_{real}\right) + K_D\frac{N}{1+N\frac{1}{s}}\left(c\cdot\gamma_{ref}-\gamma_{real}\right) \quad (14)$$

Due to the co-simulation environment, automated tuning tools could not be used. The controller was manually tuned, with a starting set derived from a Ziegler-Nichols strategy, that was then tuned through an iterative process to achieve a robust balance between tracking performance and control effort across all maneuvers. The final gains are presented in Table 6.

TABLE 6 PID tuned gains.

Parameter	Value
K_P	20.5
K_I	5.0
K_D	0.0012
N	100

© de Carvalho Pinheiro and Carello

3.3.2. Linear Quadratic Regulator The LQR is an optimal control method based on a state-space representation of the system. The bicycle model, with an external yaw moment input (M_z), was used for the state-space formulation

$$\dot{x} = Ax + Bu \quad (15)$$

where

$$x=\begin{pmatrix}\beta\\ \gamma\end{pmatrix},\ A=\begin{pmatrix}\frac{C_f+C_r}{mv_x} & \frac{aC_f-bC_r}{mv_x^2}-1\\ \frac{aC_f-bC_r}{I_{zz}} & \frac{a^2C_f+b^2C_r}{I_{zz}v_x^2}\end{pmatrix}$$

$$u=\begin{pmatrix}\delta\\ M_z\end{pmatrix},\ B=\begin{pmatrix}-\frac{C_f}{mv_x} & 0\\ -\frac{aC_f}{I_{zz}} & \frac{1}{I_{zz}}\end{pmatrix}$$

A significant challenge in applying LQR to vehicle dynamics is that the state matrices A and B are dependent on the longitudinal velocity, v_x. To address this, a gain-scheduling approach was adopted. The optimal state feedback gain matrix, K, which minimizes the cost function

$$J=\frac{1}{2}\int_0^\infty\left(x^TQx+u^TRu\right)dt \quad (16)$$

was calculated offline for a range of speeds from 0 to 100 km/h. During online simulation, the controller uses the instantaneous vehicle speed to linearly interpolate between these pre-computed gain matrices, providing a quasi-optimal solution across the operating range. After a tuning process that involved the testing of different relative values for the R and Q elements, aiming both a reduction of the overall value of J and a qualitative analysis

of the vehicle's physical response, the final weighting matrices were selected as

$$R = \begin{bmatrix} 1e^5 & 0 \\ 0 & 1 \end{bmatrix}, \; Q = 1e^6 \begin{bmatrix} 1 & 0 \\ 0 & 1000 \end{bmatrix} \tag{17}$$

The high penalty on the steering angle input in the R matrix effectively decouples the LQR's action, ensuring it primarily manipulates the yaw moment, M_z. The high penalty on the yaw rate error in the Q matrix prioritizes tracking performance.

3.3.3. First-Order SMC Two common First-Order SMC (FOSM) strategies were implemented to address the chattering phenomenon inherent in discontinuous controllers. Both use the sliding surface

$$S = \gamma_{ref} - \gamma_{real} \tag{18}$$

- **FOSM with Low-Pass Filter:** The first approach applies a simple low-pass filter to the output of a standard signum-based controller. This method smooths the control signal, attenuating the high-frequency components that cause chattering. The final control law, with a time constant of 0.5 s, found to be the best compromise between chattering attenuation and the delays introduced by the low-pass filter, is given by

$$u = \frac{1}{0.5s + 1} \cdot k_r \cdot sign\left(S\right) \tag{19}$$

- **FOSM with Continuous Signal:** The second approach replaces the discontinuous sign (S) function with a continuous saturation function that approximates its behavior

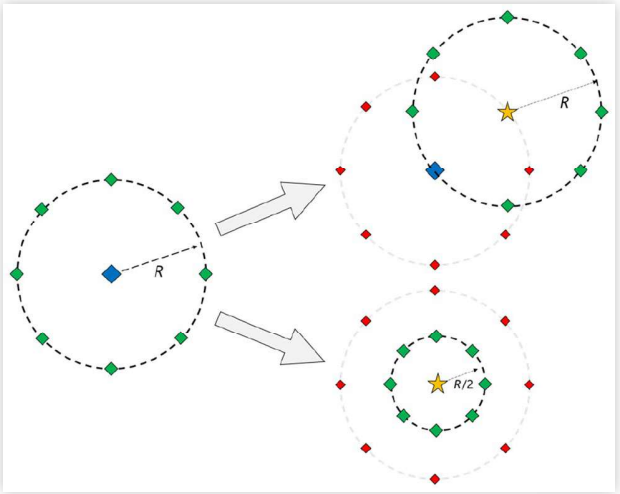
$$cont\left(S\right) = \frac{S}{|S| + \phi} \tag{20}$$

The parameter ϕ is a small positive constant: lower positive values are less smooth but closer to the signum function, larger values create a smoother result at the expense of slower and less accurate control action. A value of ϕ = 2.5 was found to provide the best trade-off between chattering reduction and tracking accuracy.

3.3.4. Second-Order SMC To further improve performance and eliminate chattering, two second-order sliding mode algorithms were implemented. SOSM controllers act on the first derivative of the control signal, resulting in a continuous final output, which is highly desirable for mechanical systems.

- **Twisting Algorithm:** This well-established SOSM algorithm is characterized by a control law that switches based on the state of both S and its derivative, $\dot{S}$ [67].

FIGURE 8 Optimization scheme for SOSM twisting algorithm.



© de Carvalho Pinheiro and Carello

The implementation follows the form

$$\dot{u} = \begin{cases} -\alpha_m sign\left(S(t)\right), & \text{when } S \cdot \dot{S} \le 0 \\ -\alpha_M sign\left(S(t)\right), & \text{when } S \cdot \dot{S} > 0 \end{cases} \tag{21}$$

The gains were obtained with an optimization-assisted and manual tuning processes composed of a sort of "neighbor search optimization" (Figure 8).

The algorithm is initialized with:

- A first guess of coefficients α_M and α_m, represented as their normalized cartesian position by the blue shape in the left.
- A factor R, representing the initial search radius.
- And an integer number of search points n, equally distributed over the circumference (green points).

Then, the simulation is run for all the n + 1 points, and the OP of each version is computed. From this point, there are two options:

- **Top right corner**: The **best** OP (star) is one of the **green** points ➔ Take this point as the new guess and repeat the process with the same R and n.
- **Bottom right corner**: The **best** OP (star) is the initial **blue** point ➔ Maintain the guess and repeat the process with a smaller R and possibly different n.

The optimization stops when R is sufficiently low, a target OP is achieved, or a number of predetermined steps is performed.

The results, after some iterations of optimization with different initial guesses and a final manual adjustment finds α_M = 16.1 and α_m = 2.8 as the tuned coefficients.

- **Suboptimal Algorithm:** This algorithm, derived from time-optimal control theory [68], aims for a monotonic convergence to the sliding surface.

  Its control law is

$$\dot{u}(t) = -k_r sign\left[S(t) - \frac{1}{2}S(t_{Mk})\right] \tag{22}$$

where t_{Mk} represents the time of the last peak of S (i.e., last occurrence of $\dot{S} = 0$). In the discrete-time implementation, this was detected by a change in the sign of $\dot{S}$ between two timesteps.

Following the procedure in [14], the gain was tuned to $k_r = I_{zz} \cdot 0.4$.

4. Results and Discussion

This section presents a comparative analysis of the six TV controllers across the full suite of evaluation maneuvers. The discussion is structured to move from a high-level qualitative assessment to a detailed quantitative comparison and a synthesis of the key performance trade-offs. The complete results for all controllers across all nine maneuvers are provided in Appendix for reference.

All the results are obtained by applying the described controllers in the simulation platform containing the PerfECT Design Tool framework, in a co-simulation environment between Simulink and VI-CarRealTime.

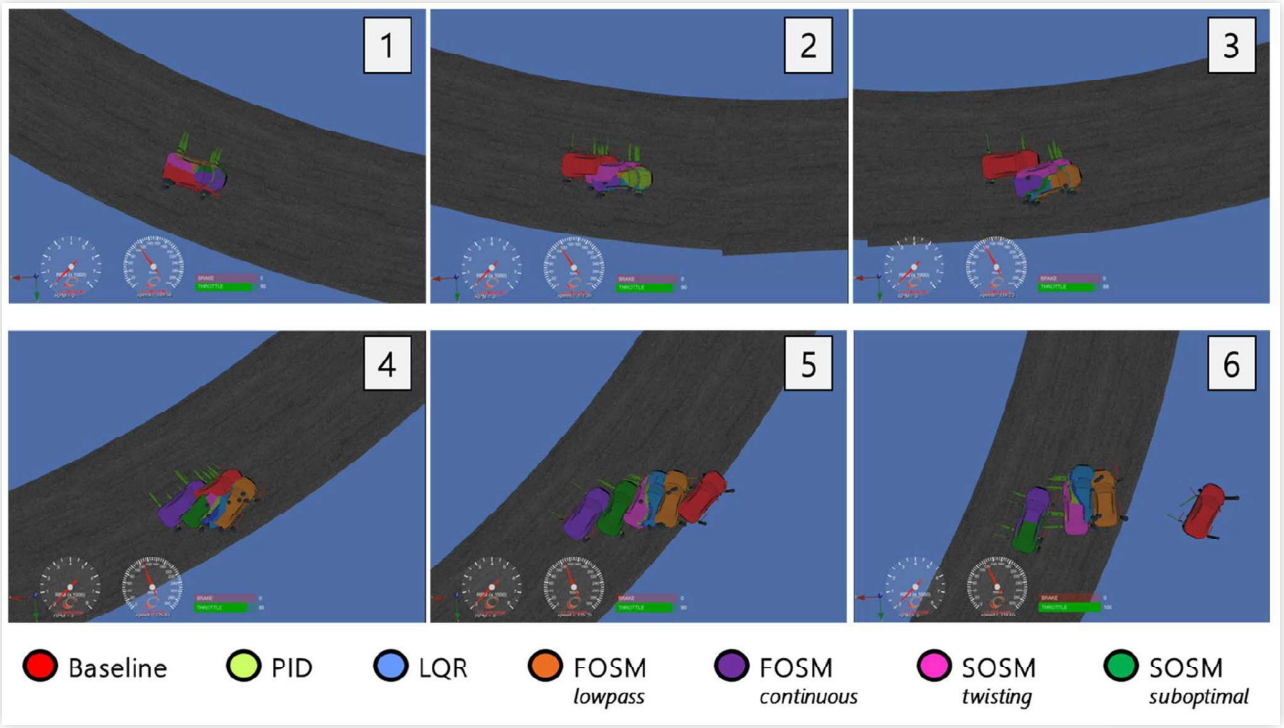
4.1. Qualitative Analysis of Limit-Handling Behavior

A qualitative overview of the controllers' effectiveness can be gained by visualizing their behavior during the most demanding phase of the CRC maneuver #1, as the vehicle approaches its limit of adhesion. Figure 9 presents a sequence of frames from the simulation (extracted using the post-processing tool VI-Animator, associated with the VI-CarRealTime environment), comparing the trajectory and attitude of the vehicle under each control strategy against the uncontrolled Baseline.

In the initial frames (1–3), all vehicles follow the target trajectory with reasonable precision. However, as the speed increases toward 120 km/h, the limitations of the Baseline vehicle become apparent. It begins to exhibit significant understeer, drifting wide of the centerline as its front tires saturate. In contrast, all controlled vehicles maintain the desired trajectory for longer, demonstrating the fundamental benefit of TV in generating a corrective yaw moment to balance the vehicle.

By the final frames (4–6), the differences between the controllers become visible. While all prevent the gross instability of the Baseline vehicle, their ability to maintain the tightest line and a stable attitude varies. The FOSM

FIGURE 9 Graphical analysis of Baseline vehicles and all classic controllers.



© de Carvalho Pinheiro and Carello

© de Carvalho Pinheiro and Carello

TABLE 7 Performance metrics for all controllers and Baseline vehicle during step steering #1.

Control	Control penalty	Error penalty	Timed penalty	Overall penalty	SSE	OS	ΔSOC (%)	Max C (A)	Max β (rad)
Baseline	0	22.31	71.32	4.84	0.91	0.94	−0.035	54.91	0.05
PID	336.97	2.40	6.32	**1.00**	0.98	0.98	−0.038	61.03	0.06
LQR	661.31	0.46	0.88	1.07	1.00	1.02	−0.040	64.51	0.06
FOSM *low-pass*	862.45	18.70	50.29	5.19	1.00	1.12	−0.042	77.36	0.10
FOSM *continuous*	344.15	2.40	7.12	1.02	0.97	0.99	−0.038	60.91	0.06
SOSM *twisting*	383.98	3.42	5.79	1.23	1.00	1.00	−0.038	62.71	0.06
SOSM *suboptimal*	703.96	0.08	0.11	1.06	1.00	1.01	−0.039	63.79	0.06

continuous and SOSM suboptimal controllers appear to manage the saturation phase most effectively, maintaining a path closest to the centerline with a visibly smaller sideslip angle. This initial visual analysis suggests that while all controllers offer a substantial improvement over the Baseline, their performance at the absolute limit of handling is not uniform.

4.2. Transient Performance

A quantitative comparison of the controllers' transient performance is presented in Table 7. This table consolidates the key metrics for the 70 km/h step steer test, providing a clear basis for comparison.

The primary function of the controllers is to track the reference yaw rate. In this regard, the LQR and SOSM suboptimal controllers demonstrate superior performance, exhibiting the lowest EP and TEP values. The SOSM suboptimal controller is particularly effective, with an EP value of just 0.08, indicating near-perfect tracking. This is also reflected in their ability to eliminate steady-state error (SSE = 1.00) with minimal overshoot (OS ≈ 1.01). The benchmark PID controller provides good performance, though its EP is significantly higher than the top performers. The FOSM low-pass controller performs poorly in this test, with a very high EP and a significant overshoot of 12%, suggesting that the filtering required to control chattering excessively slows its response.

The superior tracking performance of the LQR and SOSM suboptimal controllers comes at a clear and quantifiable cost. These two controllers exhibit the highest CP values (661 and 704, respectively), indicating a much more aggressive and energy-intensive control action. This direct link between control effort and energy use is a key finding of this study, made visible by the integrated simulation methodology. The high CP values correlate directly with a greater negative change in the battery's SOC (ΔSOC of −0.040% and −0.039%), which is approximately 5% higher than the energy consumed by the PID controller (−0.038%). This demonstrates a tangible trade-off: achieving the highest level of precision requires a measurable increase in energy consumption, which would directly impact vehicle range. The FOSM continuous controller offers a compelling balance, achieving tracking performance comparable to the PID controller with a nearly identical CP and energy consumption. The correlation between CP and maximum current is also coherent, showing a more demanding current needed for LQR and Suboptimal controllers, which might lead to an earlier saturation in case of limited EM or battery performance.

4.3. Steady-State and Limit Performance

The CRC maneuver is designed to assess the controllers' ability to improve the vehicle's handling balance and extend its performance envelope. The summary results for the most demanding CRC test #1 are presented in Table 8.

TABLE 8 Performance metrics for all controllers and Baseline vehicle during CRC #1.

Control	Control penalty	Error penalty	Timed penalty	Overall penalty	Max V (km/h)	Max a_y (g)	Avg δ (rad)	ΔSOC (%)	Max C (A)	Max e_V (km/h)
Baseline	0.0	2212.9	71,415.0	75.99	112.98	1.03	0.49	−0.695	375.86	10.85
PID	5164	15.1	449.8	**1.00**	116.7	1.01	0.40	−0.727	335.05	10.55
LQR	5490	11.9	361.6	0.93	116.8	1.01	0.39	−0.727	336.37	10.73
FOSM *low-pass*	6078	299.0	9964.0	10.93	113.8	1.03	0.38	−0.709	345.85	9.88
FOSM *continuous*	4156	50.0	1580.0	2.11	116.5	1.01	0.40	−0.725	339.49	10.90
SOSM *twisting*	5830	328.7	11,042.1	11.95	114.2	1.02	0.39	−0.712	341.53	9.55
SOSM *suboptimal*	7205	3.5	120.8	0.82	116.7	1.01	0.39	−0.727	335.65	10.65

© de Carvalho Pinheiro and Carello

All controllers significantly improve the Baseline vehicle's performance. The most direct measure of improved steering responsiveness is the average steering angle (Avg. δ) required to negotiate the corner. All controllers reduce this value from 0.49 rad (Baseline) to approximately 0.39–0.40 rad, confirming their effectiveness in counteracting the vehicle's inherent understeer. This translates to a higher maximum stable speed (Max V), with most controllers allowing the vehicle to reach more than 116 km/h compared to Baseline's 113 km/h.

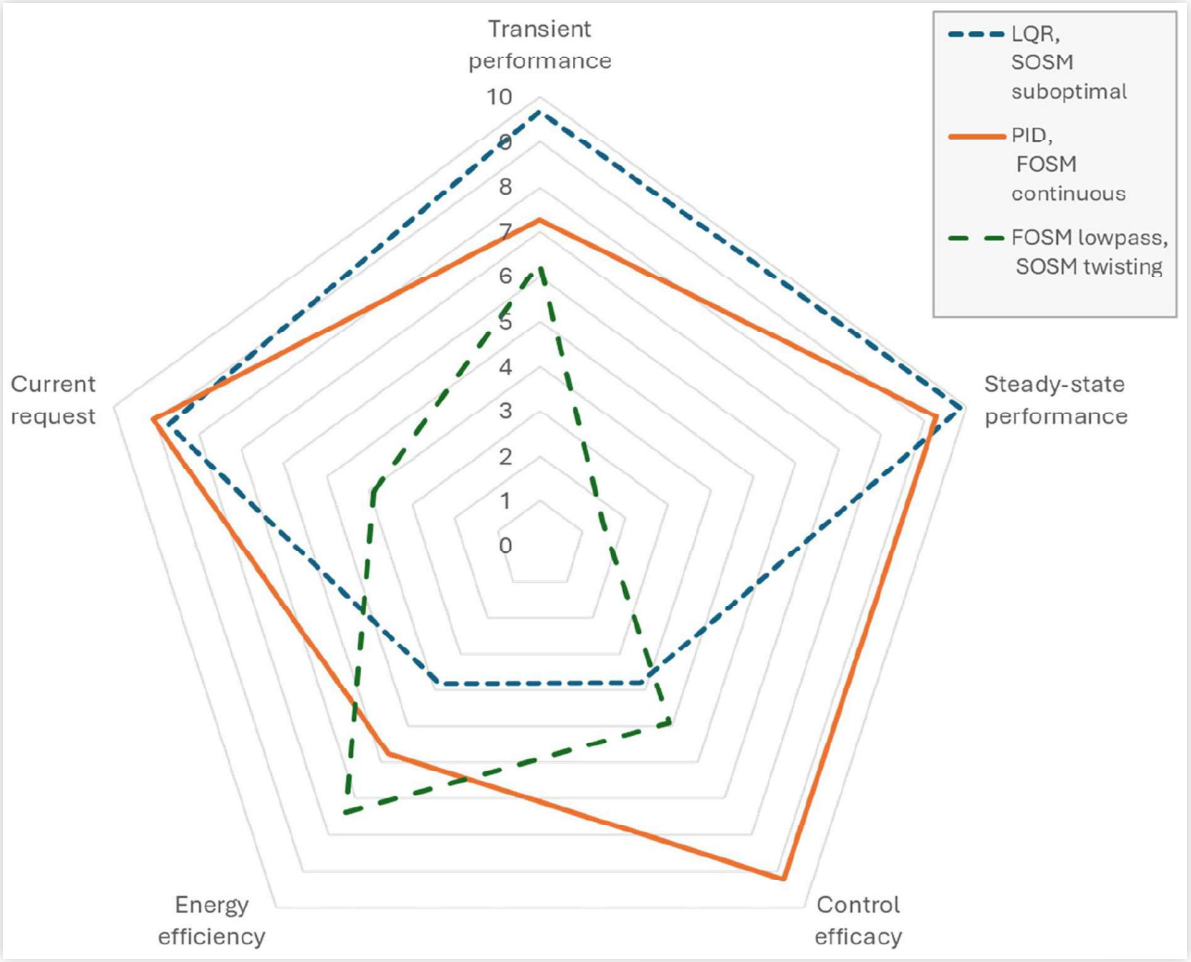
Like the transient tests, the SOSM suboptimal and LQR controllers again prove to be the most accurate, with by far the lowest EP and TEP values. In this high-load scenario, their superior performance also translates into the best OP scores (0.82 and 0.93, respectively), as the significant reduction in yaw error outweighs their higher control effort. The FOSM and SOSM twisting algorithms perform very poorly in this maneuver, with OP scores an order of magnitude higher than the benchmark PID. This suggests that these specific SMC implementations struggle to maintain control in high-g, combined-loading scenarios.

Once again, the trade-off between performance and energy is evident. The SOSM suboptimal controller, while being the top performer dynamically, also has the highest CP (= 7205) and a corresponding ΔSOC of −0.727%. This is the same energy consumption as the PID and LQR controllers, but for a much higher level of control effort, indicating that while the *corrective yaw moment* is high, the overall powertrain operation is managed efficiently. This highlights the complexity of the energy–dynamics relationship, which can only be captured by an integrated model.

4.4. Trade-Off Analysis

The results from both transient and steady-state maneuvers reveal a clear hierarchy and a distinct set of trade-offs among the controllers. To synthesize these findings, Figure 10 presents a radar chart that visualizes the average normalized performance of each controller group across several key metrics. The chart illustrates the central finding of this work: there is no single "best" controller,

FIGURE 10 Controller comparison radar chart.



© de Carvalho Pinheiro and Carello

but rather a spectrum of solutions with different strengths. The controllers were grouped according to their overall performance, as listed:

- **High-precision, high-cost (LQR, SOSM suboptimal):** These controllers excel at yaw rate tracking in all conditions. They are the best choice when the absolute priority is maximizing dynamic response and stability. However, this precision is achieved through high control effort, resulting in a measurable increase in energy consumption.
- **Balanced performance (PID, FOSM continuous):** The PID controller serves as an excellent benchmark, providing robust and predictable performance across all tests without excessive control effort or energy use. It represents a safe and effective middle-ground solution. The FOSM continuous demonstrates performance similar to the PID but with slightly lower control effort in some cases. It effectively mitigates chattering without the significant performance degradation seen in the low-pass filter variant, making it a viable and efficient alternative.
- **Underperformers (FOSM low-pass, SOSM twisting):** These controllers proved less effective in this application. The FOSM low-pass was too slow for effective transient control, while the SOSM twisting algorithm struggled under high-load steady-state cornering.

This analysis, made possible by the high-fidelity vehicle and powertrain model, provides a practical framework for controller selection. The choice of controller is not merely an algorithmic decision but a strategic one that depends on the desired balance between ultimate dynamic performance and overall vehicle energy efficiency, a critical consideration in the design of any battery electric vehicle.

5. Conclusion

This study presented a comprehensive comparison of six distinct TV control strategies for a four-wheel-independent-drive electric vehicle. The investigation was conducted using an integrated, high-fidelity simulation platform that coupled a multi-body vehicle dynamics model with detailed electro-thermal models of the powertrain and ESS. This approach was adopted to address a critical gap in the existing literature, where TV controllers are typically evaluated using simplified models that neglect the crucial influence of powertrain dynamics and energy efficiency.

The results of the comparative analysis revealed a clear and quantifiable trade-off between dynamic performance and energy consumption. The LQR and the SOSM suboptimal controllers consistently delivered the highest tracking precision and vehicle stability, particularly in demanding transient and limit-handling maneuvers. However, this superior dynamic performance was achieved at the cost of higher control effort and a measurable increase in energy consumption, as indicated by the direct correlation between the CP metric and the change in battery SOC. Conversely, the benchmark PID controller and the FOSM continuous controller offered a robust balance, providing significant handling improvements over the Baseline vehicle without incurring a substantial energy penalty. The other SMC strategies, namely the FOSM with a low-pass filter and the SOSM with the twisting algorithm, proved less suitable for this application, exhibiting either slow transient response or poor performance in high-load conditions.

The central implication of this work is that for the practical development of EVs, the selection and calibration of active chassis control systems such as TV should not be based on dynamic performance metrics alone.

The findings underscore the advantages of employing integrated, multi-domain simulation tools during the design process. Such tools are beneficial for understanding and optimizing the complex interplay between vehicle dynamics, control system aggression, and overall energy efficiency. This approach ensures that enhancements in stability and handling do not inadvertently compromise vehicle range or place undue stress on powertrain components, a critical consideration for system integration and reliability.

Future research can proceed along three main paths: the development of more advanced control systems, such as adaptive or machine learning–based controllers [69], that explicitly incorporate energy efficiency and powertrain state awareness into their control laws; validating the findings experimentally, through Hardware-in-the-Loop (HiL) and Driver-in-the-Loop (DiL) testing, followed by implementation on a prototype vehicle; and investigation of the long-term effects of different control strategies on component health, particularly the impact of aggressive torque commands on battery State of Health (SoH) degradation, providing a more complete picture of the life-cycle performance of TV systems.

Acknowledgements

The authors would like to thank Dr. Elisabetta Punta, Beond Srl and VI-Grade for the technical support for this work.

Declaration of AI-Assisted Technologies

During the preparation of this work, the authors used Google Gemini in order to assist with manuscript editing,

for example, for rephrasing sentences, finding and correcting grammar errors, and identifying format inconsistencies. After using this tool, the authors reviewed and edited the content as needed and take full responsibility for the content of the publication.

Contact Information

Henrique de Carvalho Pinheiro, corresponding author
Department of Mechanical and Aerospace engineering (DIMEAS) - Politecnico di Torino
Corso Duca degli Abruzzi 24, 10129, Turin, Italy
henrique.decarvalho@polito.it
Phone: +39 011 090 5692

List of Acronyms and Symbols

4WID - Four-Wheel-Independent-Drive
BMS - Battery Management System
CoG - Center of Gravity
CRC - Constant Radius Cornering
DOF - Degree of Freedom
DYC - Direct Yaw Control
EM - Electric Motor
EMRAX - Brand name, no specific acronym meaning
IWM - In-Wheel Motor
LQR - Linear Quadratic Regulator
MPC - Model Predictive Control
NDOB - Nonlinear Disturbance Observer
OP - Overall Penalty
PI - Proportional–Integral
PID - Proportional–Integral–Derivative
SMC - Sliding Mode Control
SOC - State of Charge
SWA - Steering Wheel Angle
TEP - Timed Error Penalty
TV - Torque Vectoring

Symbol	Meaning	Units
β	Sideslip angle	rad
γ	Yaw rate	rad/s
δ	Steering angle	rad or °
SWA	Steering wheel angle	rad or °
a_x	Longitudinal acceleration	m/s^2 or g
a_y	Lateral acceleration	m/s^2 or g
l	Wheelbase	m
a	Distance from CoG to front axle	m
b	Distance from CoG to rear axle	m
C_f	Front tire cornering stiffness	N/rad
C_r	Rear tire cornering stiffness	N/rad
$I_{i,j}$	Yaw moment of inertia around i,j direction	kg·m^2
u_x	Longitudinal speed	m/s
V	Total vehicle speed	m/s
M_z	External yaw moment	Nm
m	Vehicle total mass	kg
m_{LF}	Mass over the left-front tire	kg
m_{RF}	Mass over the right-front tire	kg
m_{LR}	Mass over the left-rear tire	kg
m_{RR}	Mass over the right-rear tire	kg
$m_{U,F}$	Unsprung mass over the front axle	kg
$m_{U,R}$	Unsprung mass over the rear axle	kg
m_S	Total sprung mass	kg
K_U	Understeering coefficient	—
T^*	Torque reference	Nm
T_λ	Torque reference after flux saturation	Nm
T_p	Torque reference after ESS power saturation	Nm
T_v	Torque reference after voltage saturation	Nm
T_{EM}	Electric machine torque output	Nm
x_{EM}	Electric machine state	—
x_{ESS}	Energy storage system state	—
$\lambda_{dqs,\,lim}$	Flux limitation	Wb
v_{ds}, v_{qs}	Quadrature voltages	V
OP	Overall penalty	—
CP	Control penalty	—
EP	Error penalty	—
TEP	Timed error penalty	—
W_{CP}	Weight for control penalty	—
W_{EP}	Weight for error penalty	—
W_{TEP}	Weight for timed error penalty	—
e	Control error	—
u	Control action	—
K_P	Proportional gain	—
K_I	Integral gain	—
K_D	Derivative gain	—
N	Filter constant	—
x	State vector	—
A	State matrix	—
B	Control matrix	—
K	Control gain matrix	—
J	Cost Function	—
Q	State weighting matrix	—
R	Control weighting matrix	—
s	Laplace operator variable	
S	Sliding surface	—
ϕ	Smoothing constant	—
t_{Mk}	Suboptimal algorithm: time of the last peak of S	s
k_r, α_m, α_M	SMC gains	—

References

1. Terashima, M., Ashikaga, T., Mizuno, T., Natori, K. et al., "Novel Motors and Controllers for High-Performance Electric Vehicle with Four In-Wheel Motors," *IEEE Transactions on Industrial Electronics* 44, no. 1 (1997): 28-38, doi:https://doi.org/10.1109/41.557496.
2. Furukawa, Y. and Abe, M., "Direct Yaw Moment Control with Estimating Side-Slip Angle by Using On-Board-Tire-Model," in *AVEC (Advance Vehicle Control)*, Nagoya, Japan, 1998.
3. Abe, M., Kano, Y., Shibahata, Y., and Furukawa, Y., "Improvement of Vehicle Handling Safety with Vehicle Side-Slip Control by Direct Yaw Moment," *Vehicle System Dynamics* 33, no. S1 (1999): 665-679, doi:https://doi.org/10.1080/00423114.1999.12063120.
4. Abe, M., Kano, A.K.A., Suzuki, K.S.K., Furukawa, Y. et al., "Estimation of vehicle side-slip angle for DYC by using on-board-tire-model," In *Proceedings of the 4th International Symposium on Advanced Vehicle Control*, AVEC '98, 14-18 September 1998, Nagoya, Japan.
5. Assadian, F. and Hancock, M., "A Comparison of Yaw Stability Control Strategies for the Active Differential," in *Proceedings of the IEEE International Symposium on Industrial Electronics, 2005. ISIE 2005*, Dubrovnik, Croatia, 373-378, 2005, doi:https://doi.org/10.1109/ISIE.2005.1528939.
6. Pugi, L., Favilli, T., Berzi, L., Locorotondo, E. et al., "Brake Blending and Torque Vectoring of Road Electric Vehicles: A Flexible Approach Based on Smart Torque Allocation," *International Journal of Electric and Hybrid Vehicles* 12, no. 2 (2020): 87-115, doi:https://doi.org/10.1504/IJEHV.2020.106339.
7. Tempone, G.P., De Carvalho Pinheiro, H., Imberti, G., and Carello, M., "Control System for Regenerative Braking Efficiency in Electric Vehicles with Electro-Actuated Brakes," SAE Technical Paper 10-08-02-0015 (2024), doi:https://doi.org/10.4271/10-08-02-0015.
8. Sakai, S., Sado, H., and Hori, Y., "Motion Control in an Electric Vehicle with Four Independently Driven In-Wheel Motors," *IEEE/ASME Transactions on Mechatronics* 4, no. 1 (1999): 9-16, doi:https://doi.org/10.1109/3516.752079.
9. Kanchwala, H., Rodriguez, P.L., Mantaras, D.A., Wideberg, J. et al., "Obtaining Desired Vehicle Dynamics Characteristics with Independently Controlled In-Wheel Motors: State of Art Review," *SAE Int. J. Passeng. Cars - Mech. Syst.* 10, no. 2 (2017): 413-425, doi:https://doi.org/10.4271/2017-01-9680.
10. Osborn, R.P. and Shim, T., "Independent Control of All-Wheel-Drive Torque Distribution," *Vehicle System Dynamics* 44, no. 7 (2006): 529-546, doi:https://doi.org/10.1080/00423110500485731.
11. Vignati, M., Sabbioni, E., and Tarsitano, D., "Torque Vectoring Control for IWM Vehicles," *International Journal of Vehicle Performance* 2, no. 3 (2016): 302-324, doi:https://doi.org/10.1504/IJVP.2016.078561.
12. Ding, S., Liu, L., and Zheng, W.X., "Sliding Mode Direct Yaw-Moment Control Design for In-Wheel Electric Vehicles," *IEEE Transactions on Industrial Electronics* 64, no. 8 (2017): 6752-6762, doi:https://doi.org/10.1109/TIE.2017.2682024.
13. Liao, Z., Cai, L., Li, J., Zhang, Y. et al., "Direct Yaw Moment Control of Eight-Wheeled Distributed Drive Electric Vehicles Based on Super-Twisting Sliding Mode Control," *Front. Mech. Eng.* 9 (2024): 1347852, doi:https://doi.org/10.3389/fmech.2023.1347852.
14. De Novellis, L., Sorniotti, A., Gruber, P., and Pennycott, A., "Comparison of Feedback Control Techniques for Torque-Vectoring Control of Fully Electric Vehicles," *IEEE Trans. Veh. Technol.* 63, no. 8 (2014): 3612-3623, doi:https://doi.org/10.1109/TVT.2014.2305475.
15. De Novellis, L., Sorniotti, A., Gruber, P., Shead, L. et al., "Torque Vectoring for Electric Vehicles with Individually Controlled Motors: State-of-the-Art and Future Developments," *World Electric Vehicle Journal* 5, no. 2 (2012): 617-628, doi:https://doi.org/10.3390/wevj5020617.
16. Goggia, T., Sorniotti, A., De Novellis, L., and Ferrara, A., "Torque-Vectoring Control in Fully Electric Vehicles via Integral Sliding Modes," in *2014 American Control Conference*, Portland, OR, 3918-3923, 2014, doi:https://doi.org/10.1109/ACC.2014.6858807.
17. Goggia, T. et al., "Integral Sliding Mode for the Torque-Vectoring Control of Fully Electric Vehicles: Theoretical Design and Experimental Assessment," *IEEE Transactions on Vehicular Technology* 64, no. 5 (2015): 1701-1715, doi:https://doi.org/10.1109/TVT.2014.2339401.
18. De Novellis, L., Sorniotti, A., and Gruber, P., "Driving Modes for Designing the Cornering Response of Fully Electric Vehicles with Multiple Motors," *Mechanical Systems and Signal Processing* 64–65 (2015): 1-15, doi:https://doi.org/10.1016/j.ymssp.2015.03.024.
19. De Novellis, L., Sorniotti, A., Gruber, P., Orus, J. et al., "Direct Yaw Moment Control Actuated through Electric Drivetrains and Friction Brakes: Theoretical Design and Experimental Assessment," *Mechatronics* 26 (2015): 1-15, doi:https://doi.org/10.1016/j.mechatronics.2014.12.003.
20. Pennycott, A., De Novellis, L., Sabbatini, A., Gruber, P. et al., "Reducing the Motor Power Losses of a Four-Wheel Drive, Fully Electric Vehicle via Wheel Torque Allocation," *Proceedings of the Institution of Mechanical Engineers, Part D: Journal of Automobile Engineering* 228, no. 7 (2014): 830-839, doi:https://doi.org/10.1177/0954407013516106.
21. Zha, Y., Quan, X., Ma, F., Liu, G. et al., "Stability Control for a Four-Wheel-Independent-Drive Electric Vehicle Based on Model Predictive Control," *SAE Int. J. Veh. Dyn., Stab., and NVH* 5, no. 2 (2021): 191-204, doi:https://doi.org/10.4271/10-05-02-0013.
22. Wang, Z., Wang, Y., Zhang, L., and Liu, M., "Vehicle Stability Enhancement through Hierarchical Control for a Four-Wheel-Independently-Actuated Electric Vehicle," *Energies* 10, no. 7 (2017): 947, doi:https://doi.org/10.3390/en10070947.

23. Wang, J. and Li, J., "Hierarchical Coordinated Control Method of In-Wheel Motor Drive Electric Vehicle Based on Energy Optimization," *World Electric Vehicle Journal* 10, no. 2 (2019): 15, doi:https://doi.org/10.3390/wevj10020015.
24. Liu, S., Zhang, H., Wang, S., and Zhao, X., "Hierarchical Torque Vectoring Control Strategy of Distributed Driving Electric Vehicles Considering Stability and Economy," *Sensors* 25, no. 13 (2025): 3933, doi:https://doi.org/10.3390/s25133933.
25. Kim, S.H. and Kim, K.-K.K., "Model Predictive Control for Energy-Efficient Yaw-Stabilizing Torque Vectoring in Electric Vehicles With Four In-Wheel Motors," *IEEE Access* 11 (2023): 37665-37680, doi:https://doi.org/10.1109/ACCESS.2023.3266330.
26. Kang, Q., Meng, D., Jiang, Y., Zhao, C. et al., "Torque Vectoring Control of Distributed Drive Electric Vehicles Using Fast Iterative Model Predictive Control," *IFAC-PapersOnLine* 58, no. 29 (2024): 106-111, doi:https://doi.org/10.1016/j.ifacol.2024.11.128.
27. Canale, M., Fagiano, L., Ferrara, A., and Vecchio, C., "Vehicle Yaw Control via Second-Order Sliding-Mode Technique," *IEEE Transactions on Industrial Electronics* 55, no. 11 (2008): 3908-3916, doi:https://doi.org/10.1109/TIE.2008.2003200.
28. Cho, J. and Huh, K., "Torque Vectoring System Design for Hybrid Electric–All Wheel Drive Vehicle," *Proceedings of the Institution of Mechanical Engineers, Part D: Journal of Automobile Engineering* 234, no. 10–11 (2020): 2680-2692, doi:https://doi.org/10.1177/0954407020906626.
29. Xu, X., Xiong, L., and Feng, Y., "Torque Vectoring Control for Handling Improvement of 4WD EV," *Advanced Materials Research* 765–767 (2013): 1893-1898, doi:https://doi.org/10.4028/www.scientific.net/AMR.765-767.1893.
30. Siampis, E., Velenis, E., and Longo, S., "Predictive Rear Wheel Torque Vectoring Control with Terminal Understeer Mitigation Using Nonlinear Estimation," in *2015 54th IEEE Conference on Decision and Control (CDC)*, Osaka, Japan, 4302-4307, 2015, doi:https://doi.org/10.1109/CDC.2015.7402890.
31. Tota, A., Lenzo, B., Qian, L., Sorniotti, A. et al., "On the Experimental Analysis of Integral Sliding Modes for Yaw Rate and Sideslip Control of an Electric Vehicle with Multiple Motors," *International Journal of Automotive Technology* 19 (2018): 811-823, doi:https://doi.org/10.1007/s12239-018-0078-0.
32. Siampis, E., Velenis, E., and Longo, S., "Model Predictive Torque Vectoring Control for Electric Vehicles Near the Limits of Handling," in *2015 European Control Conference (ECC)*, Linz, Austria, 2553-2558, 2015, doi:https://doi.org/10.1109/ECC.2015.7330922.
33. Chae, M., Hyun, Y., Yi, K., and Nam, K., "Dynamic Handling Characteristics Control of an In-Wheel-Motor Driven Electric Vehicle Based on Multiple Sliding Mode Control Approach," *IEEE Access* 7 (2019): 132448-132458, doi:https://doi.org/10.1109/ACCESS.2019.2940434.
34. Canale, M., Fagiano, L., Ferrara, A., and Vecchio, C., "Comparing Internal Model Control and Sliding-Mode Approaches for Vehicle Yaw Control," *IEEE Transactions on Intelligent Transportation Systems* 10, no. 1 (2009): 31-41, doi:https://doi.org/10.1109/TITS.2008.2006772.
35. de Carvalho Pinheiro, H., Punta, E., Carello, M., Ferraris, A. et al., "Torque Vectoring in Hybrid Vehicles with In-Wheel Electric Motors: Comparing SMC and PID Control," in *2021 IEEE International Conference on Environment and Electrical Engineering and 2021 IEEE Industrial and Commercial Power Systems Europe (EEEIC/I CPS Europe)*, Bari, Italy, 1-6, 2021, doi:https://doi.org/10.1109/EEEIC/ICPSEurope51590.2021.9584732.
36. Montani, M., Favilli, T., Berzi, L., Capitani, R. et al., "ESC on In-Wheel Motors Driven Electric Vehicle: Handling and Stability Performances Assessment," in *2020 IEEE International Conference on Environment and Electrical Engineering and 2020 IEEE Industrial and Commercial Power Systems Europe (EEEIC/I CPS Europe)*, Bari, Italy, 1-6, 2020, doi:https://doi.org/10.1109/EEEIC/ICPSEurope49358.2020.9160768.
37. Favilli, T., Pugi, L., Berzi, L., and Pierini, M., "Coordinated Steering and Torque Vectoring Lateral Stability Sliding Mode Control Applied to an Electric In-Wheel Motors Vehicle," in *2021 IEEE International Conference on Environment and Electrical Engineering and 2021 IEEE Industrial and Commercial Power Systems Europe (EEEIC/I CPS Europe)*, Bari, Italy, 1-6, 2021, doi:https://doi.org/10.1109/EEEIC/ICPSEurope51590.2021.9584717.
38. Ferraris, A., de Carvalho Pinheiro, H., Galanzino, E., Airale, A.G., and Carello, M., "All-Wheel Drive Electric Vehicle Performance Optimization: From Modelling to Subjective Evaluation on a Static Simulator," in *2019 Electric Vehicles International Conference, EV 2019*, Bucharest, Romania, 2019, doi:https://doi.org/10.1109/EV.2019.8893027.
39. Aouadj, N., Hartani, K., and Fatiha, M., "New Integrated Vehicle Dynamics Control System Based on the Coordination of Active Front Steering, Direct Yaw Control, and Electric Differential for Improvements in Vehicle Handling and Stability," *SAE Int. J. Veh. Dyn., Stab., and NVH* 4, no. 2 (2020): 119-133, doi:https://doi.org/10.4271/10-04-02-0009.
40. Davoudi, M., "A Fuzzy Based Vehicle Dynamic Stability Control (FDSC)," SAE Technical Paper 2006-01-3483 (2006), doi:https://doi.org/10.4271/2006-01-3483.
41. Ferrara, A., Incremona, G.P., and Regolin, E., "Optimization-Based Adaptive Sliding Mode Control with Application to Vehicle Dynamics Control: Optimization-Based Adaptive SMC with Application to Vehicle Dynamics Control," *Int. J. Robust Nonlinear Control* 29, no. 3 (2019): 550-564, doi:https://doi.org/10.1002/rnc.4105.
42. Mousaei, A. and Naderi, Y., "Optimal Predictive Torque Distribution Control System to Enhance Stability and

Energy Efficiency in Electric Vehicles," *Sustainability* 15, no. 20 (2023): 15155, doi:https://doi.org/10.3390/su152015155.

43. Valdivieso-Soto, A., Galluzzi, R., Tramacere, E., Cespi, R. et al., "Lyapunov-Based Pitch Control for Electric Vehicles Using In-Wheel Motors," *Vehicles* 7, no. 2 (2025): 37, doi:https://doi.org/10.3390/vehicles7020037.
44. Zhao, B., Lou, B., He, X., Xue, W. et al., "Optimal Torque Vectoring Control for Autonomous Electric Vehicles Considering Ride Comfort," SAE Technical Paper 2025-01-8310 (2025), doi:https://doi.org/10.4271/2025-01-8310.
45. Zheng, Z., Cao, W., Kubota, Y., Nakano, Y. et al., "Robust and Energy-Efficient Torque Vectoring for a Four In-Wheel Motor Electric Vehicle Based on Sliding Mode and Model Predictive Control," *Un. Sys.* 13, no. 06 (2025): 1699-1712, doi:https://doi.org/10.1142/S2301385025430022.
46. Adeleke, O.P., Li, Y., Chen, Q., Zhou, W. et al., "Torque Distribution Based on Dynamic Programming Algorithm for Four In-Wheel Motor Drive Electric Vehicle Considering Energy Efficiency Optimization," *World Electric Vehicle Journal* 13, no. 10 (2022): 181, doi:https://doi.org/10.3390/wevj13100181.
47. De Carvalho Pinheiro, H., "PerfECT Design Tool: Electric Vehicle Modelling and Experimental Validation," *World Electric Vehicle Journal* 14, no. 12 (2023): 337, doi:https://doi.org/10.3390/wevj14120337.
48. Milliken, W.F., *Race Car Vehicle Dynamics* (Warrendale, PA: Society of Automotive Engineers, 1995), ISBN:978-0-7680-0103-7
49. Grano, E., Bianco, E., De Carvalho Pinheiro, H., and Carello, M., "MTPA and Flux Weakening Control of Electric Motors: A Numerical Approach," in *2023 IEEE International Conference on Environment and Electrical Engineering and 2023 IEEE Industrial and Commercial Power Systems Europe (EEEIC/I&CPS Europe)*, Madrid, Spain, 1-7, 2023, doi:https://doi.org/10.1109/EEEIC/ICPSEurope57605.2023.10194684.
50. Grano, E., de Carvalho Pinheiro, H., and Carello, M., "A Novel Electric Drive Description to Bridge the Gap between Energetic and Equivalent-Circuit Models," *Proceedings of the Institution of Mechanical Engineers, Part D: Journal of Automobile Engineering* (2025): 09544070251330340, doi:https://doi.org/10.1177/09544070251330340.
51. Grano, E., Lazek, T., Carello, M., Grano, E. et al., "A numerical Methodology for Induction Motor Control: Lookup Tables Generation and Steady-State Performance Analysis," SAE Technical Paper 2024-01-2152 (2024), doi:https://doi.org/10.4271/2024-01-2152.
52. Muhlethaler, J., Biela, J., Kolar, J.W., and Ecklebe, A., "Core Losses under the DC Bias Condition Based on Steinmetz Parameters," *IEEE Transactions on Power Electronics* 27, no. 2 (2012): 953-963, doi:https://doi.org/10.1109/TPEL.2011.2160971.
53. EMRAX, "Technical Data and Manual for EMRAX Motors/Generators," 2018, accessed May 03, 2023, https://emrax.com/wp-content/uploads/2017/10/user_manual_for_emrax_motors.pdf.
54. Carello, M., De Carvalho Pinheiro, H., Messana, A., Freedman, A. et al., "Composite Control Arm Design: A Comprehensive Workflow," *SAE Int. J. Adv. & Curr. Prac. in Mobility* 3, no. 5 (2021): 2355-2369, doi:https://doi.org/10.4271/2021-01-0364.
55. Brest, J.-S. and Gimbert, Y., "Influence of In-Wheel Motors Weight on a Swing-Arm Dynamic, Evaluation of Ride Comfort and Handling," *World Electric Vehicle Journal* 8, no. 1 (2016): 112-121, doi:https://doi.org/10.3390/wevj8010112.
56. Anderson, M.J., "Unsprung Mass with In-Wheel Motors-Myths and Realities," in *10th International Symposium on Advanced Vehicle Control*, Loughborough, UK, 2010.
57. Vos, R., Besselink, I.J.M., and Nijmeijer, H., "Influence of In-Wheel Motors on the Ride Comfort of Electric Vehicles," in *Proceedings of the 10th International Symposium on Advanced Vehicle Control (AVEC10)*, Loughborough, UK, 835-840, 2010.
58. Cuadrado, J., Vilela, D., Iglesias, I., Martin, A., and Peña, A., "A Multibody Model to Assess the Effect of Automotive Motor In-Wheel Configuration on Vehicle Stability and Comfort," in *ECCOMAS Multibody Dynamics 2013*, Zagreb, Croatia, 2013.
59. Zuraulis, V., Kojis, P., Marotta, R., Šukevičius, Š. et al., "Electric Vehicle Corner Architecture: Driving Comfort Evaluation Using Objective Metrics," SAE Technical Paper 2022-01-0921 (2022), doi:https://doi.org/10.4271/2022-01-0921.
60. Woo, S. and Shin, D., "A Double Sky-Hook Algorithm for Improving Road-Holding Property in Semi-Active Suspension Systems for Application to In-Wheel Motor," *Applied Sciences* 11, no. 19 (2021): 8912, doi:https://doi.org/10.3390/app11198912.
61. Suzuki, T., Chauvicourt, F., and Fujimoto, H., "High-Bandwidth Suspension Resonance Analysis of In-Wheel Motor Vehicle Using Multibody Dynamics," in *2021 IEEE International Conference on Mechatronics (ICM)*, Kashiwa, Japan, 1-6, 2021, doi:https://doi.org/10.1109/ICM46511.2021.9385653.
62. Hott, L., Ivanov, V., Augsburg, K., Ricciardi, V. et al., "Ride Blending Control for AWD Electric Vehicle with In-Wheel Motors and Electromagnetic Suspension," in *2020 IEEE Vehicle Power and Propulsion Conference (VPPC)*, Gijon, Spain, 1-5, 2020, doi:https://doi.org/10.1109/VPPC49601.2020.9330946.
63. Geng, C., Uchida, T., and Hori, Y., "Body Slip Angle Estimation and Control for Electric Vehicle with In-Wheel Motors," in *IECON 2007—33rd Annual Conference of the IEEE Industrial Electronics Society*, Taipei, Taiwan, 351-355, 2007, doi:https://doi.org/10.1109/IECON.2007.4460281.
64. De Martino, M., Farroni, F., Pasquino, N., Sakhnevych, A. et al., "Real-Time Estimation of the Vehicle Sideslip Angle

through Regression Based on Principal Component Analysis and Neural Networks," in *2017 IEEE International Systems Engineering Symposium (ISSE)*, Vienna, Austria, 1-6, 2017, doi:https://doi.org/10.1109/SysEng.2017.8088274.

65. Chindamo, D., Gadola, M., Bonera, E., and Magri, P., "Experimental Comparison of The Two Most Used Vehicle Sideslip Angle Estimation Methods for Model-Based Design Approach," *J. Phys.: Conf. Ser.* 1888, no. 1 (2021): 012006, doi:https://doi.org/10.1088/1742-6596/1888/1/012006.
66. Nishio, A., Tozu, K., Yamaguchi, H., Asano, K. et al., "Development of Vehicle Stability Control System Based on Vehicle Sideslip Angle Estimation," SAE Technical Paper 2001-01-0137 (2001), doi:https://doi.org/10.4271/2001-01-0137.
67. Bartolini, G., Pisano, A., Punta, E., and Usai, E., "A Survey of Applications of Second-Order Sliding Mode Control to Mechanical Systems," *International Journal of Control* 76, no. 9–10 (2003): 875-892, doi:https://doi.org/10.1080/00207170310000099010.
68. Bartolini, G., Ferrara, A., and Usai, E., "Applications of a Sub-Optimal Discontinuous Control Algorithm for Uncertain Second Order Systems," *International Journal of Robust and Nonlinear Control* 7, no. 4 (1997): 299-319, doi:https://doi.org/10.1002/(SICI)1099-1239(199704)7:4%3C299::AID-RNC279%3E3.0.CO;2-3.
69. de Carvalho Pinheiro, H. and Carello, M., "Reinforcement Learning Based Control for Torque Allocation in Electric Vehicles: A Preliminary Analysis," in *2024 International Conference on Artificial Intelligence, Computer, Data Sciences and Applications (ACDSA)*, 1-6, 2024, doi:https://doi.org/10.1109/ACDSA59508.2024.10467491.

Appendix: Simulation Results

In this Appendix the complete results of the simulations are reported, both as relevant plots and as comparison tables of the performance factors previously described, during all nine maneuvers including step steering and CRC events. The results refer, respectively, to Baseline, PID, LQR, FOSM low-pass, FOSM continuous, SOSM twisting, and SOSM suboptimal.

TABLE A.1 Baseline vehicle—Step steering performance evaluation.

Step	CP	EP	TEP	OP	SSE	OS	ΔSOC (%)	Max C	Max β
1	0	22.31	71.32	4.84	0.91	0.94	−0.035	54.91	0.05
2	0	59.48	200.16	13.07	0.85	0.91	−0.043	69.19	0.06
3	0	1.26	3.11	0.26	0.97	0.98	−0.022	27.31	0.01
4	0	26.79	77.74	5.69	0.90	0.96	−0.038	57.07	0.05
5	0	1.24	3.48	0.26	1.02	1.03	−0.015	18.90	0.00

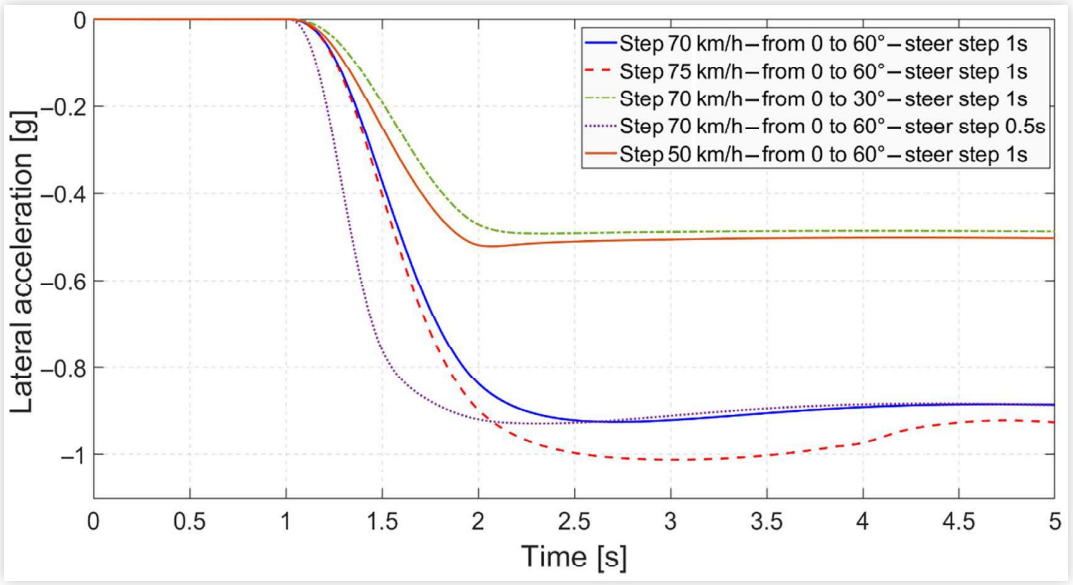
© de Carvalho Pinheiro and Carello

TABLE A.2 Baseline vehicle—CRC performance evaluation.

CRC	CP	EP	TEP	OP	Max V	Max a_y	Avg δ	ΔSOC (%)	Max C	Max e_y
1	0.0	2213.0	71,415.3	76.0	112.98	1.03	0.49	−0.695	375.9	10.8
2	0.0	4586.9	81,691.1	142.5	113.63	1.03	0.63	−0.599	296.4	7.4
3	0.0	4468.7	45,904.8	131.2	114.10	1.03	0.83	−0.569	437.4	12.4
4	0.0	600.3	2576.1	16.8	111.60	1.00	0.41	−0.017	131.6	6.0

© de Carvalho Pinheiro and Carello

FIGURE A.1 PID control—Step steering vehicle response.



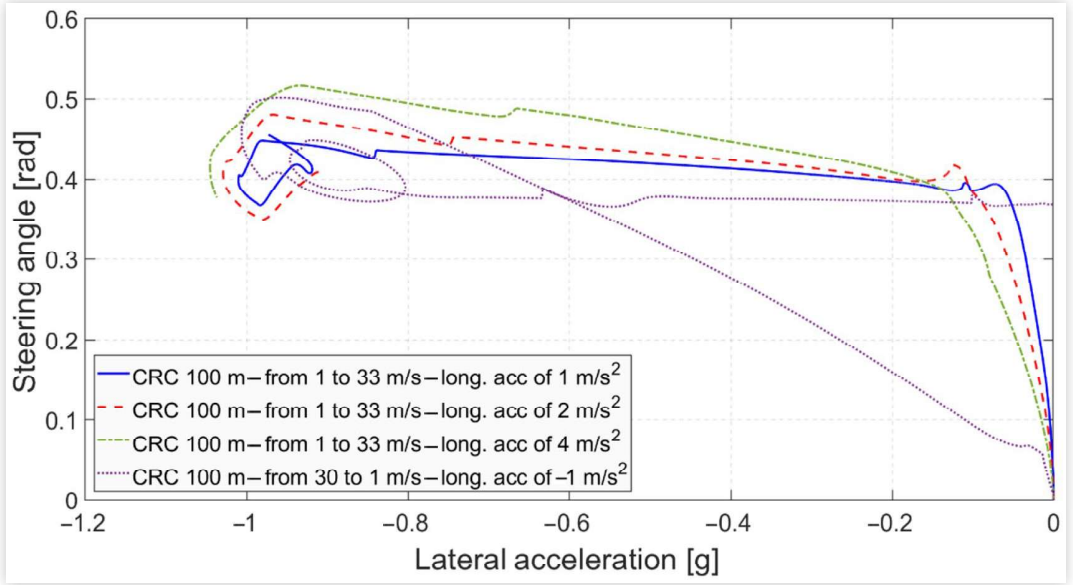
© de Carvalho Pinheiro and Carello

TABLE A.3 PID control—Step steering performance evaluation.

Step	CP	EP	TEP	OP	SSE	OS	ΔSOC (%)	Max C	Max β
1	336.97	2.40	6.32	1.00	0.98	0.98	−0.038	61.03	0.06
2	522.53	4.01	12.12	1.63	0.96	0.98	−0.044	99.44	0.09
3	36.92	0.29	0.60	0.11	0.99	0.99	−0.022	27.67	0.02
4	425.03	3.36	7.31	1.31	0.98	0.99	−0.041	63.67	0.06
5	34.69	0.43	1.14	0.14	1.01	1.02	−0.015	18.90	0.00

© de Carvalho Pinheiro and Carello

FIGURE A.2 PID control—CRC vehicle response.



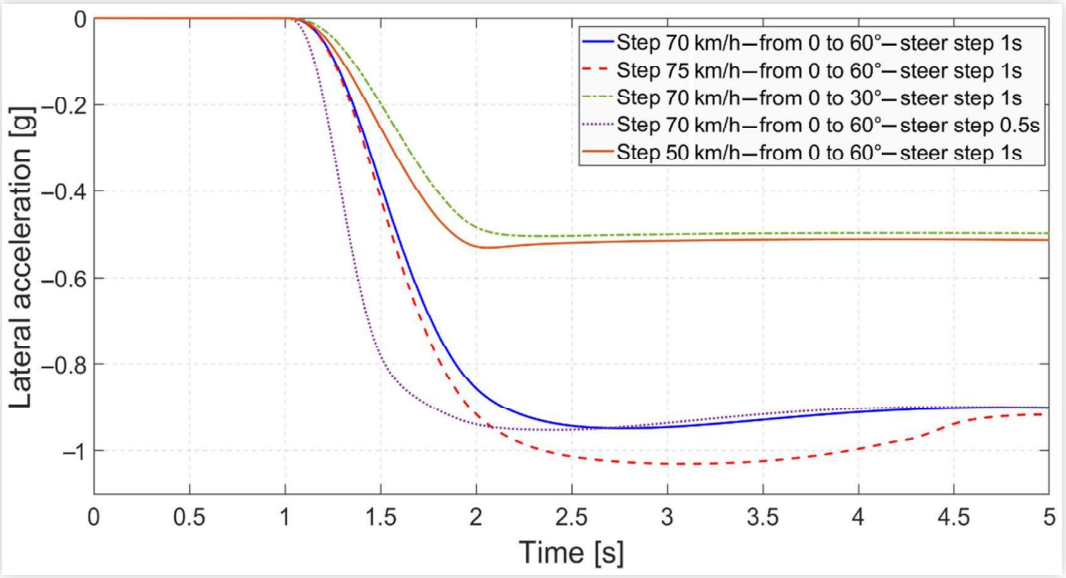
© de Carvalho Pinheiro and Carello

TABLE A.4 PID control—CRC performance evaluation.

CRC	CP	EP	TEP	OP	Max V	Max a_y	Avg δ	ΔSOC (%)	Max C	Max e_V
1	5164	15.1	449.8	1.00	116.7	1.01	0.40	−0.727	335.05	10.55
2	2965	15.3	230.2	0.75	113.9	1.04	0.42	−0.561	414.87	11.80
3	2801	21.0	176.7	0.88	115.2	1.06	0.47	−0.545	437.43	12.43
4	2609	9.6	65.3	0.53	111.6	1.01	0.38	−0.015	136.17	6.74

© de Carvalho Pinheiro and Carello

FIGURE A.3 LQR control—Step steering vehicle response.



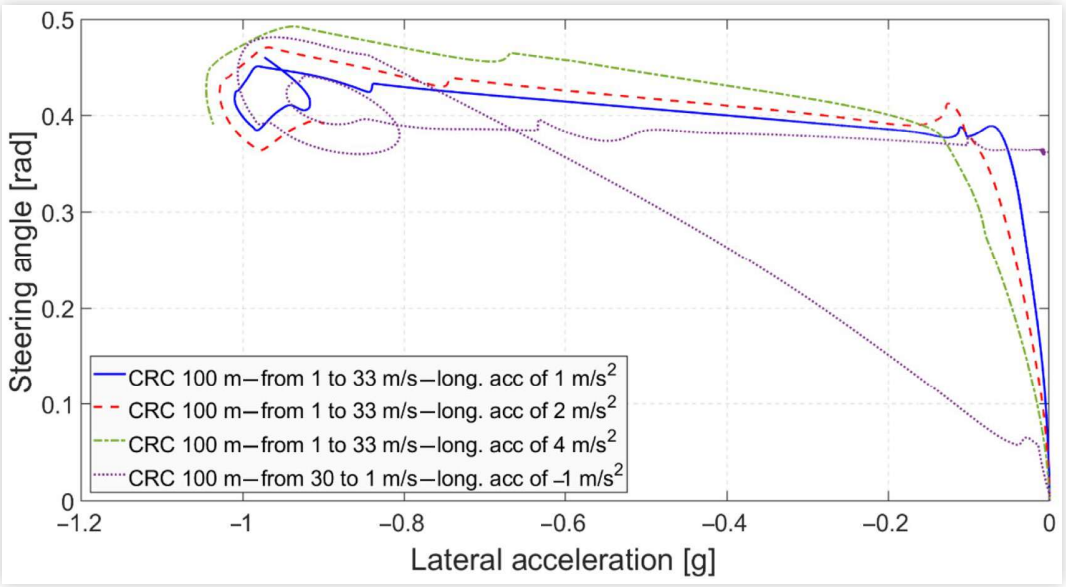
© de Carvalho Pinheiro and Carello

TABLE A.5 LQR control—Step steering performance evaluation.

Step	CP	EP	TEP	OP	SSE	OS	ΔSOC (%)	Max C	Max β
1	661.31	0.46	0.88	1.07	1.00	1.02	−0.040	64.51	0.06
2	791.46	1.06	2.85	1.40	0.99	1.02	−0.043	113.60	0.11
3	138.77	0.13	0.33	0.23	1.01	1.02	−0.023	28.03	0.02
4	810.01	1.03	1.49	1.40	1.00	1.02	−0.044	67.15	0.07
5	56.28	1.48	5.00	0.41	1.03	1.03	−0.015	19.02	0.00

© de Carvalho Pinheiro and Carello

FIGURE A.4 LQR control—CRC vehicle response.



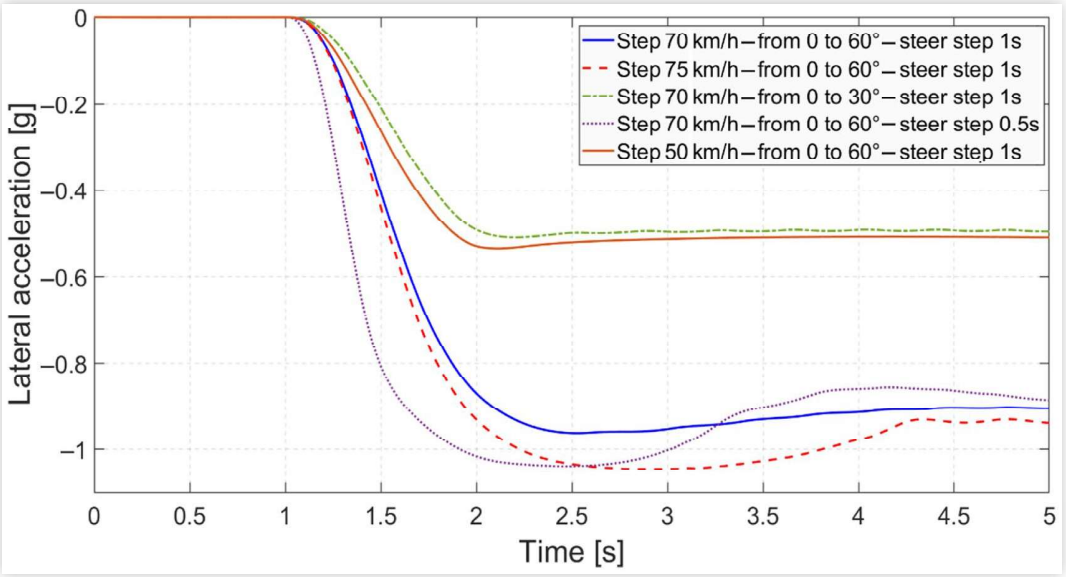
© de Carvalho Pinheiro and Carello

TABLE A.6 LQR control—CRC performance evaluation.

CRC	CP	EP	TEP	OP	Max V	Max a_y	Avg δ	ΔSOC (%)	Max C	Max e_V
1	5490	11.9	361.6	0.93	116.8	1.01	0.39	−0.727	336.37	10.73
2	3486	7.5	115.8	0.57	113.9	1.04	0.41	−0.562	415.47	11.93
3	3356	8.7	74.3	0.58	115.1	1.06	0.45	−0.543	437.67	12.43
4	2578	4.2	46.3	0.37	111.6	1.01	0.38	−0.015	135.33	6.61

© de Carvalho Pinheiro and Carello

FIGURE A.5 FOSM low-pass control—Step steering vehicle response.



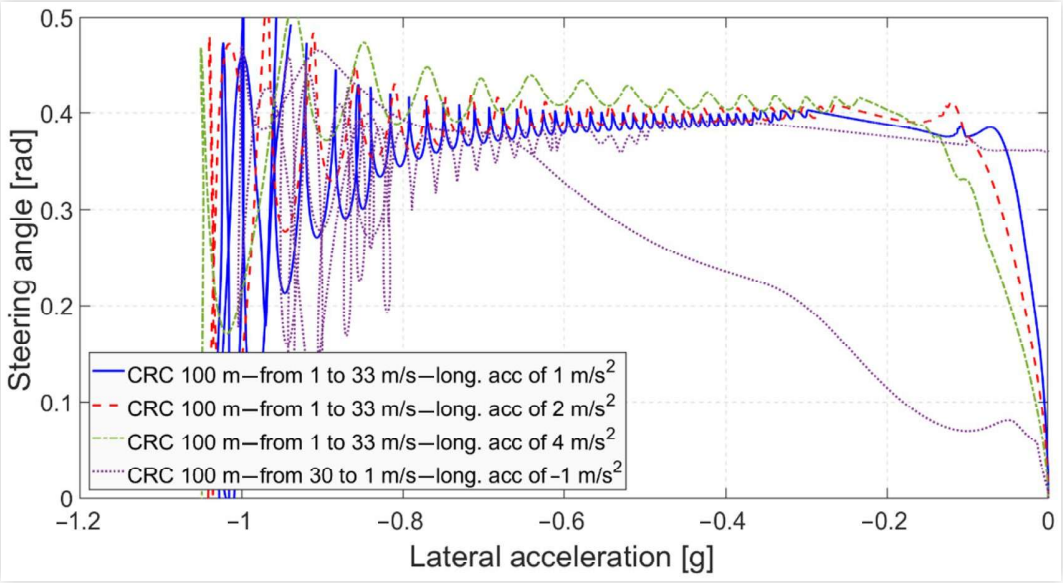
© de Carvalho Pinheiro and Carello

TABLE A.7 FOSM low-pass control—Step steering performance evaluation.

Step	CP	EP	TEP	OP	SSE	OS	ΔSOC (%)	Max C	Max β
1	862.45	18.70	50.29	5.19	1.00	1.12	−0.042	77.36	0.10
2	1372.97	141.62	459.32	32.89	1.04	1.26	−0.066	143.25	0.26
3	153.87	0.19	0.42	0.27	0.99	1.04	−0.023	27.91	0.02
4	623.68	7.66	12.27	2.40	1.00	1.06	−0.044	68.59	0.08
5	139.78	2.62	8.09	0.77	1.03	1.07	−0.015	19.02	0.00

© de Carvalho Pinheiro and Carello

FIGURE A.6 FOSM low-pass control—CRC vehicle response.



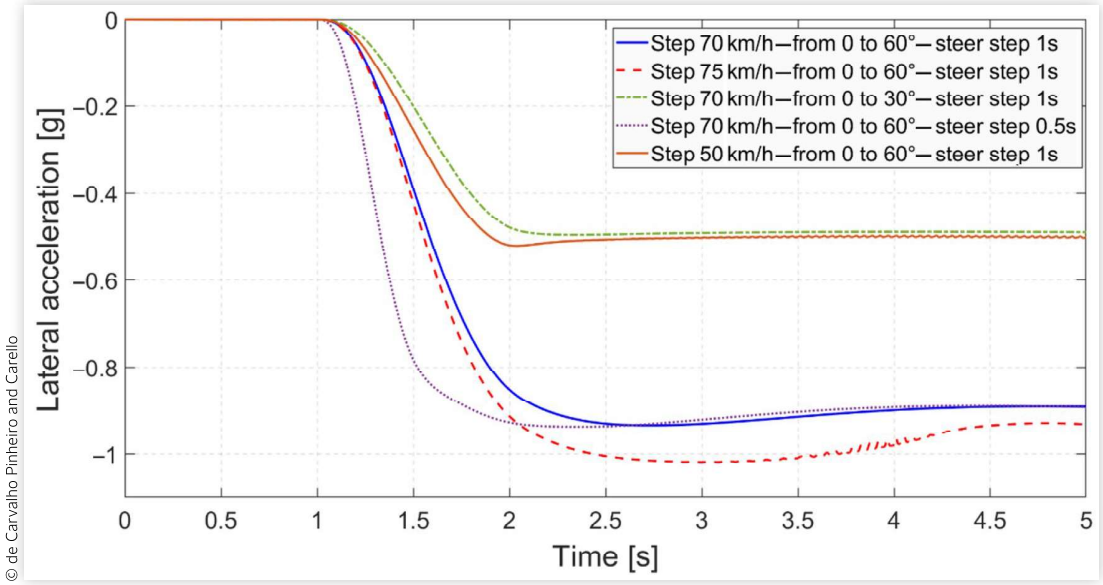
© de Carvalho Pinheiro and Carello

TABLE A.8 FOSM low-pass control—CRC performance evaluation.

CRC	CP	EP	TEP	OP	Max V	Max a_y	Avg δ	ΔSOC (%)	Max C	Max e_V
1	6078	299.0	9964.0	10.93	113.8	1.03	0.38	−0.709	345.85	9.88
2	5146	494.6	8842.7	15.87	114.6	1.05	0.36	−0.576	314.29	10.39
3	5072	545.6	5622.8	16.51	115.5	1.07	0.34	−0.551	438.27	12.42
4	3302	28.9	139.6	1.13	111.6	1.01	0.37	−0.015	134.01	6.37

© de Carvalho Pinheiro and Carello

FIGURE A.7 FOSM continuous control—Step steering vehicle response.



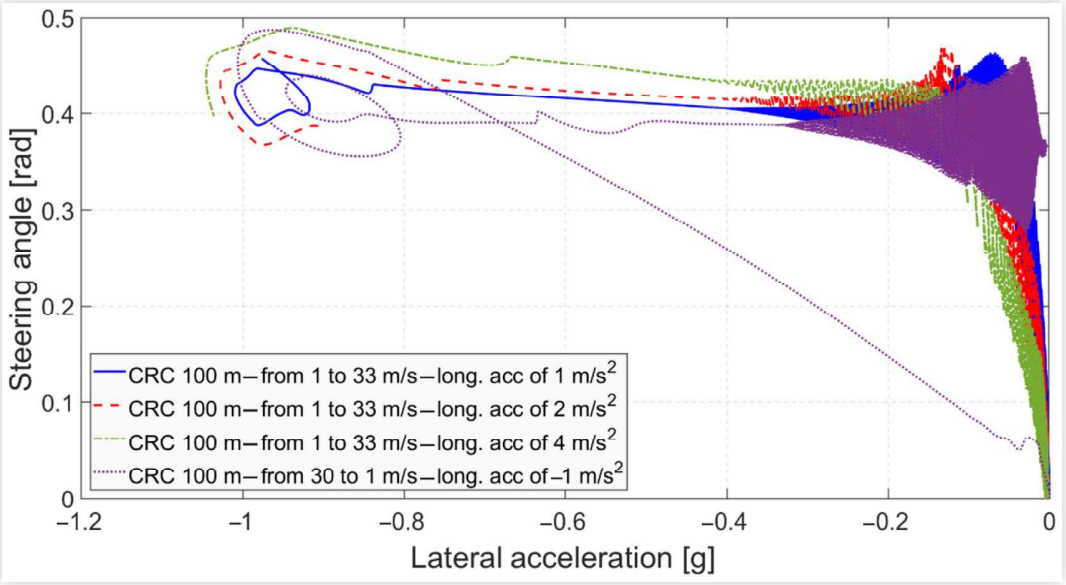
© de Carvalho Pinheiro and Carello

TABLE A.9 FOSM continuous control—Step steering performance evaluation.

Step	CP	EP	TEP	OP	SSE	OS	ΔSOC (%)	Max C	Max β
1	344.15	2.40	7.12	1.02	0.97	0.99	−0.038	60.91	0.06
2	532.25	4.23	14.06	1.72	0.95	0.98	−0.044	98.24	0.09
3	41.60	0.24	0.57	0.11	0.99	0.99	−0.022	27.67	0.02
4	425.95	3.44	8.51	1.34	0.97	0.99	−0.041	63.31	0.06
5	52.26	0.30	0.82	0.14	1.01	1.01	−0.015	18.90	0.00

© de Carvalho Pinheiro and Carello

FIGURE A.8 FOSM continuous control—Step steering vehicle response.



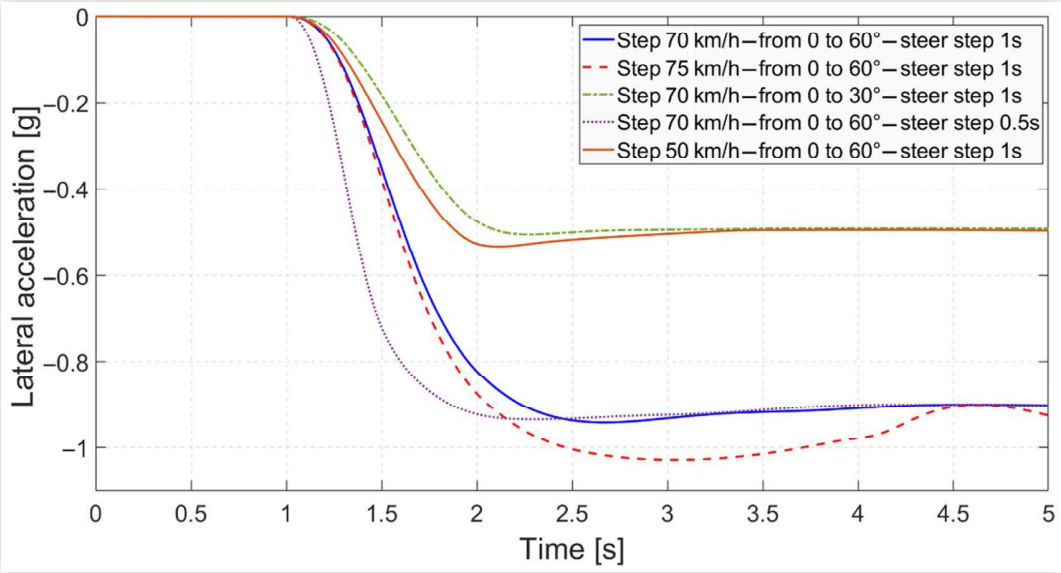
© de Carvalho Pinheiro and Carello

TABLE A.10 FOSM continuous control—CRC performance evaluation.

CRC	CP	EP	TEP	OP	Max V	Max a_y	Avg δ	ΔSOC (%)	Max C	Max e_V
1	4156	50.0	1580.0	2.11	116.5	1.01	0.40	−0.725	339.49	10.90
2	2567	30.3	474.0	1.17	114.1	1.04	0.43	−0.557	333.25	12.17
3	2605	41.4	364.4	1.45	115.4	1.06	0.48	−0.552	437.07	12.43
4	1972	15.8	88.3	0.64	111.6	1.01	0.39	−0.015	136.29	6.76

© de Carvalho Pinheiro and Carello

FIGURE A.9 SOSM twisting control—Step steering vehicle response.



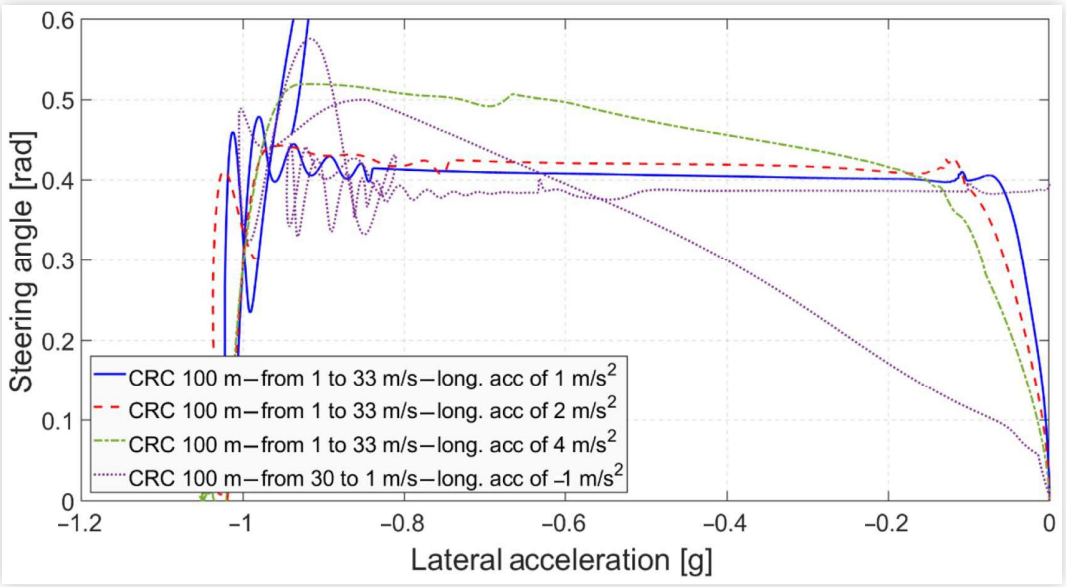
© de Carvalho Pinheiro and Carello

TABLE A.11 SOSM twisting control—Step steering performance evaluation.

Step	CP	EP	TEP	OP	SSE	OS	ΔSOC (%)	Max C	Max β
1	383.98	3.42	5.79	1.23	1.00	1.00	−0.038	62.71	0.06
2	352.72	9.96	28.48	2.63	0.98	1.00	−0.042	103.88	0.10
3	60.48	0.44	0.67	0.17	1.00	1.02	−0.022	27.79	0.02
4	425.46	6.49	8.78	1.85	1.00	1.00	−0.042	65.23	0.06
5	86.56	0.67	1.30	0.26	1.00	1.04	−0.015	18.78	0.00

© de Carvalho Pinheiro and Carello

FIGURE A.10 SOSM twisting control—CRC vehicle response.



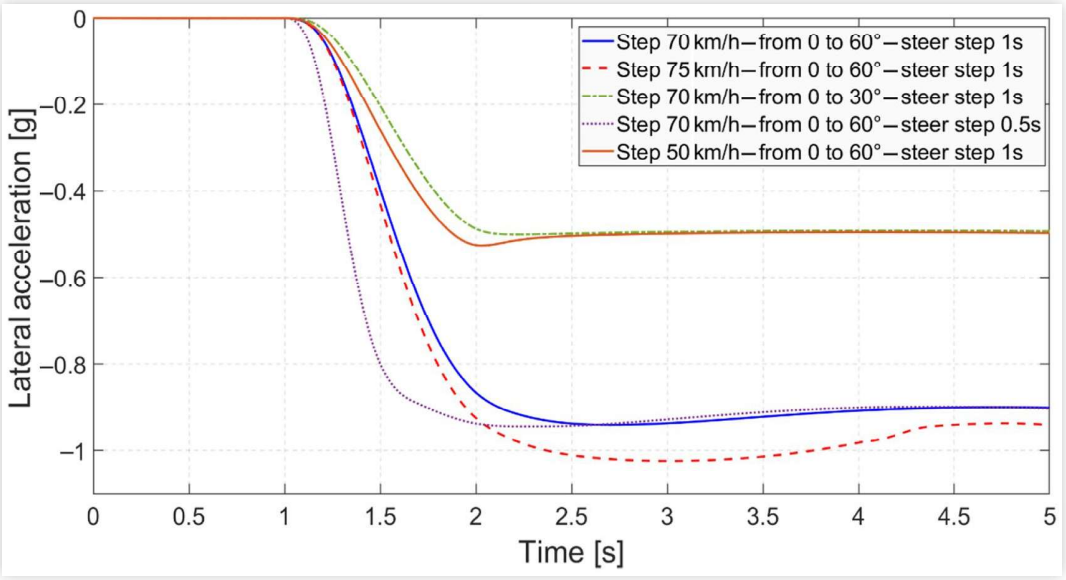
© de Carvalho Pinheiro and Carello

TABLE A.12 SOSM twisting control—CRC performance evaluation.

CRC	CP	EP	TEP	OP	Max V	Max a_y	Avg δ	ΔSOC (%)	Max C	Max e_V
1	5830	328.7	11,042.1	11.95	114.2	1.02	0.39	−0.712	341.53	9.55
2	4659	398.0	7028.0	12.80	114.1	1.04	0.37	−0.571	309.85	10.41
3	2672	580.7	5889.0	17.28	115.8	1.06	0.41	−0.560	437.07	12.43
4	3088	39.3	118.2	1.39	111.6	1.01	0.39	−0.015	134.97	6.51

© de Carvalho Pinheiro and Carello

FIGURE A.11 SOSM suboptimal control—Step steering vehicle response.



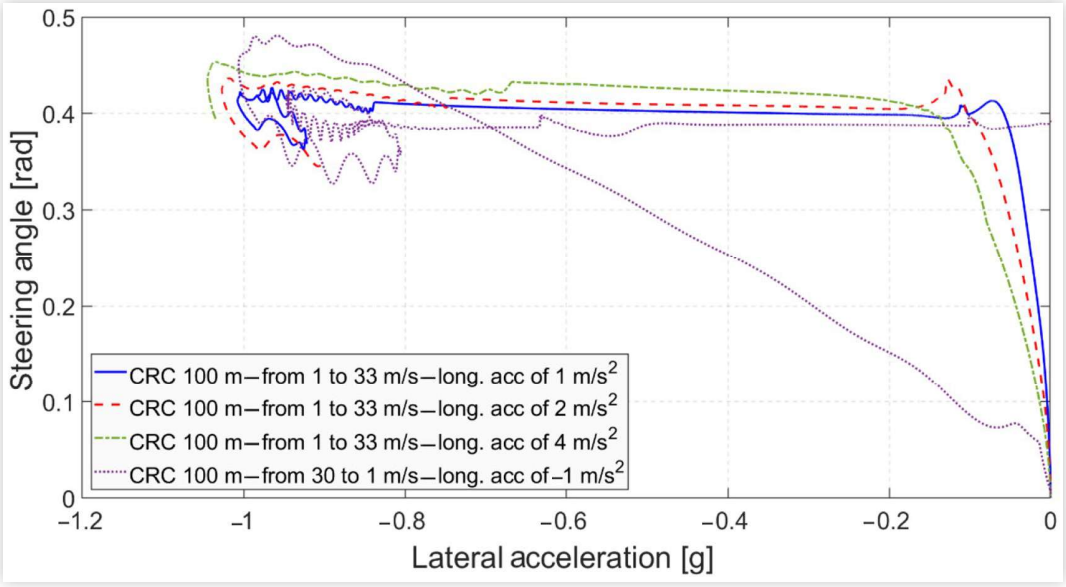
© de Carvalho Pinheiro and Carello

TABLE A.13 SOSM suboptimal control—Step steering performance evaluation.

Step	CP	EP	TEP	OP	SSE	OS	ΔSOC (%)	Max C	Max β
1	703.96	0.08	0.11	1.06	1.00	1.01	−0.039	63.79	0.06
2	957.82	0.22	0.62	1.47	1.00	1.01	−0.044	108.20	0.10
3	121.38	0.03	0.04	0.19	1.00	1.01	−0.023	27.91	0.02
4	843.00	0.65	0.79	1.37	1.00	1.03	−0.043	66.43	0.06
5	180.65	0.05	0.08	0.28	1.00	1.02	−0.015	18.78	0.00

© de Carvalho Pinheiro and Carello

FIGURE A.12 SOSM suboptimal control—CRC vehicle response.



© de Carvalho Pinheiro and Carello

TABLE A.14 SOSM suboptimal control—CRC performance evaluation.

CRC	CP	EP	TEP	OP	Max V	Max a_y	Avg δ	ΔSOC (%)	Max C	Max e_V
1	7205	3.5	120.8	0.82	116.7	1.01	0.39	−0.727	335.65	10.65
2	4628	0.9	16.6	0.48	113.8	1.03	0.41	−0.564	414.99	11.84
3	4382	0.1	1.2	0.43	115.1	1.06	0.43	−0.538	438.87	12.43
4	3863	4.1	19.9	0.49	111.6	1.01	0.39	−0.016	135.45	6.58

© de Carvalho Pinheiro and Carello

© 2026 de Carvalho Pinheiro and Carello. Published by SAE International. This Open Access article is published under the terms of the Creative Commons Attribution Non-Commercial License (http://creativecommons.org/licenses/by-nc/4.0), which permits noncommercial use, distribution, and reproduction in any medium, provided that the original author(s) and the source are credited.

Positions and opinions advanced in this work are those of the author(s) and not necessarily those of SAE International. Responsibility for the content of the work lies solely with the author(s).